

This is a repository copy of *Performance assessment of long-legged tightly-baffled divertor geometries in the ARC reactor concept*.

White Rose Research Online URL for this paper:

<https://eprints.whiterose.ac.uk/151880/>

Version: Published Version

Article:

Wigram, Michael Robert Knox, Labombard, Brian, Umansky, M. et al. (7 more authors) (2019) Performance assessment of long-legged tightly-baffled divertor geometries in the ARC reactor concept. Nuclear Fusion. 106052. pp. 1-20. ISSN 1741-4326

<https://doi.org/10.1088/1741-4326/ab394f>

Reuse

This article is distributed under the terms of the Creative Commons Attribution (CC BY) licence. This licence allows you to distribute, remix, tweak, and build upon the work, even commercially, as long as you credit the authors for the original work. More information and the full terms of the licence here:

<https://creativecommons.org/licenses/>

Takedown

If you consider content in White Rose Research Online to be in breach of UK law, please notify us by emailing eprints@whiterose.ac.uk including the URL of the record and the reason for the withdrawal request.

PAPER • OPEN ACCESS

Performance assessment of long-legged tightly-baffled divertor geometries in the ARC reactor concept

To cite this article: M.R.K. Wigram *et al* 2019 *Nucl. Fusion* **59** 106052

View the [article online](#) for updates and enhancements.








IOP | ebooks™

Bringing you innovative digital publishing with leading voices to create your essential collection of books in STEM research.

Start exploring the [collection](#) - download the first chapter of every title for free.

Performance assessment of long-legged tightly-baffled divertor geometries in the ARC reactor concept

M.R.K. Wigram¹, B. LaBombard², M.V. Umansky³, A.Q. Kuang²,
T. Golfinopoulos², J.L. Terry², D. Brunner², M.E. Rensink³, C.P. Ridgers¹
and D.G. Whyte²

¹ York Plasma Institute, Department of Physics, University of York, Heslington, York, YO10 5DD, United Kingdom of Great Britain and Northern Ireland

² MIT Plasma Science and Fusion Center, Cambridge, MA 02139, United States of America

³ Lawrence Livermore National Laboratory, Livermore, CA 94550, United States of America

E-mail: michael.wigram@gmail.com

Received 31 January 2019, revised 17 July 2019

Accepted for publication 7 August 2019

Published 12 September 2019



Abstract

Extremely intense power exhaust channels are projected for tokamak-based fusion power reactors; a means to handle them remains to be demonstrated. Advanced divertor configurations have been proposed as potential solutions. Recent modelling of tightly baffled, long-legged divertor geometries for the divertor test tokamak concept, ADX, has shown that these concepts may access passively stable, fully detached regimes over a broad range of parameters. The question remains as to how such divertors may perform in a reactor setting. To explore this, numerical simulations are performed with UEDGE for the long-legged divertor geometry proposed for the ARC pilot plant conceptual design—a device with projected heat flux power width ($\lambda_{q||}$) of 0.4 mm and power exhaust of 93 MW—first for a simplified Super-X divertor configuration (SXD) and then for the actual X-point target divertor (XPTD) being proposed. It is found that the SXD, combined with 0.5% fixed-fraction neon impurity concentration, can produce passively stable, detached divertor regimes for power exhausts in the range of 80–108 MW—fully accommodating ARC's power exhaust. The XPTD configuration is found to reduce the strike-point temperature by a factor of ~ 10 compared to the SXD for small separations ($\sim 1.4\lambda_{q||}$) between main and divertor X-point magnetic flux surfaces. Even greater potential reductions are identified for reducing separations to $\sim 1\lambda_{q||}$ or less. The power handling response is found to be insensitive to the level of cross-field convective or diffusive transport assumed in the divertor leg. By raising the separatrix density by a factor of 1.5, stable fully detached divertor solutions are obtained that fully accommodate the ARC exhaust power without impurity seeding. To our knowledge, this is the first time an impurity-free divertor power handling scenario has been obtained in edge modelling for a tokamak fusion power reactor with $\lambda_{q||}$ of 0.4 mm.

Keywords: ARC, UEDGE, divertor, power handling, detached, modelling

(Some figures may appear in colour only in the online journal)



Original content from this work may be used under the terms of the [Creative Commons Attribution 3.0 licence](https://creativecommons.org/licenses/by/3.0/). Any further distribution of this work must maintain attribution to the author(s) and the title of the work, journal citation and DOI.

1. Introduction

The divertor power handling and divertor plasma detachment control remains a major concern for both near-term experimental fusion devices as well as demonstration fusion power plant scale reactors of the future. For ITER—the next and largest fusion power experiment to date with a project generated fusion power of $P_{\text{fus}} \sim 500$ MW—modelling of the scrape-off-layer (SOL) and divertor show an unmitigated heat flux of 40 MW m^{-2} at the divertor targets [1], well above the 10 MW m^{-2} value considered to be the maximum by material limitations [2]. Mitigation techniques will be employed to bring the ITER target heat flux within 10 MW m^{-2} , including steep tilting of the divertor plates to the magnetic field geometry [1], and operating with partial divertor detachment induced using impurity seeding and high neutral pressures [3–5]. However, it is recognised that these techniques are likely to be inadequate to handle the higher heat loads expected from future reactor-level devices like DEMO [6, 7]. Moreover, in order to suppress target erosion to acceptable levels, fully detached divertor conditions may be required. Added to this requirement is a formidable divertor plasma control challenge—e.g. at no time during high power operation should the divertor plasma be allowed to re-attach to the target, despite inevitable variations in power exhaust that are associated with transients (e.g. confinement transitions).

A variety of advanced divertor configurations [8] and operational scenarios are being considered to address these challenges. Double-null operation is being considered because it may allow a sharing of heat load among upper and lower targets [9]. Extension of the divertor leg and placement of the divertor target at large major radius with increased magnetic field flaring, as in the Super-X divertor (SXD) configuration [10], has been proposed. These techniques will be implemented in the MAST-U tokamak design for an experimental assessment [11]. Complex magnetic geometries have also been proposed—including the X-divertor [12], snowflake [13] and X-point target divertors (XPTD) [14] with additional magnetic X-points within or close to the divertor plasma volume. These have been studied computationally [15, 16] and have been or are presently being explored in proof-of-concept experiments, such as in the TCV tokamak [17]. A number of these advanced divertor designs are under assessment for application to DEMO [18].

Until recently, it had been assumed that tightly baffled, long-legged divertors, would not be practical in tokamak power reactors because they would occupy too much volume inside the toroidal field coils or the arrangement of poloidal field coils needed to produce them would be incompatible with coil current limits and/or neutron shielding requirements [19]. The development of the ARC reactor design [20] (Affordable, Robust, Compact reactor) and the recent incorporation of an advanced divertor into it [22] demonstrate a new approach in which tightly baffled, long-leg divertors can be accommodated, working synergistically with the reactor design. ARC is a conceptual tokamak design for a reduced size, cost and complexity demonstration fusion pilot power plant (200–250 MWe), designed to operate at a comparable fusion power to

ITER (~ 500 MW), but at a compact size ($R_0 = 3.3$ m) comparable to JET [20]. To achieve this fusion power at a compact size, the design employs REBCO (rare earth barium copper oxide) superconducting tape for the toroidal field (TF) coils [21] to allow for high magnetic field operation ($B_0 = 9.2$ T). An added benefit of the superconducting REBCO tape material is that the higher operating temperature supports the use of resistive joints, enabling the TF coils to be demountable [21]. This allows for easy inner vessel replacement, as well as for poloidal field coils to be placed inside the TF coils while still being sufficiently shielded by the blanket to neutron damage. This is crucial as it allows for enhanced plasma shaping capabilities and the realistic implementation of advanced divertors in a reactor. A 3D design projection for the original ARC concept [20] is given in figure 1(a). An updated design incorporating a long-legged X-point target divertor [22] is shown in figure 1(b).

It is important to highlight that the long leg divertor design for ARC was implemented while keeping the TF coil dimension and core plasma volume constant, maintaining a tritium breeding ratio greater than one, and not affecting coil lifetime estimates [22]. This was achieved not only due to the demountable TF coil design but also because of the liquid FLiBe immersion blanket concept [20]. The long leg divertors were implemented by carving out space from the FLiBe blanket which allowed for the TF coil dimension and core plasma volume to be unaffected.

At first glance, one might anticipate that the divertor challenge in ARC is more severe than in lower field tokamaks due to the Eich empirical scaling law which indicates that the H-mode power decay width $\lambda_{q||}$ will be only ~ 0.4 mm [23]. However, ARC's high magnetic field allows it to attain the areal power density needed for a reactor ($\sim 2.5 \text{ MW m}^{-2}$) based on economic considerations but at significantly reduced total power levels [24] and consequently total power exhaust levels. The total exhaust power for ARC is estimated to be only ~ 93 MW [22], assuming a 35% core radiation fraction. The net effect is that the parallel heat flux entering into the divertor is expected to be similar to that of larger, low field devices that achieve similar areal power loading, despite the smaller $\lambda_{q||}$. Nevertheless, because of the formidable divertor challenge, the ARC design team sought to incorporate a tightly baffled, long leg, X-point target divertor (XPTD) into ARC's design. Modelling of this concept for the ADX divertor test tokamak indicated that it could access passively stable, fully detached divertor regimes over a broad range of parameters [25]. A factor of 10 enhancement in peak power handling compared to conventional divertors has been obtained in some cases. However, the question remained as to what performance the XPTD might actually attain in the ARC design.

This paper presents the results of a modelling study aimed at addressing precisely this question. The modelling tool used in this study is the SOL and divertor transport code UEDGE [26, 27], which was recently enhanced to handle magnetic X-points in the divertor volume [25]. At the time this study was initiated, it was not obvious to the authors that any plausible divertor heat flux handling scenario would be found for ARC, without implementing excessive levels of

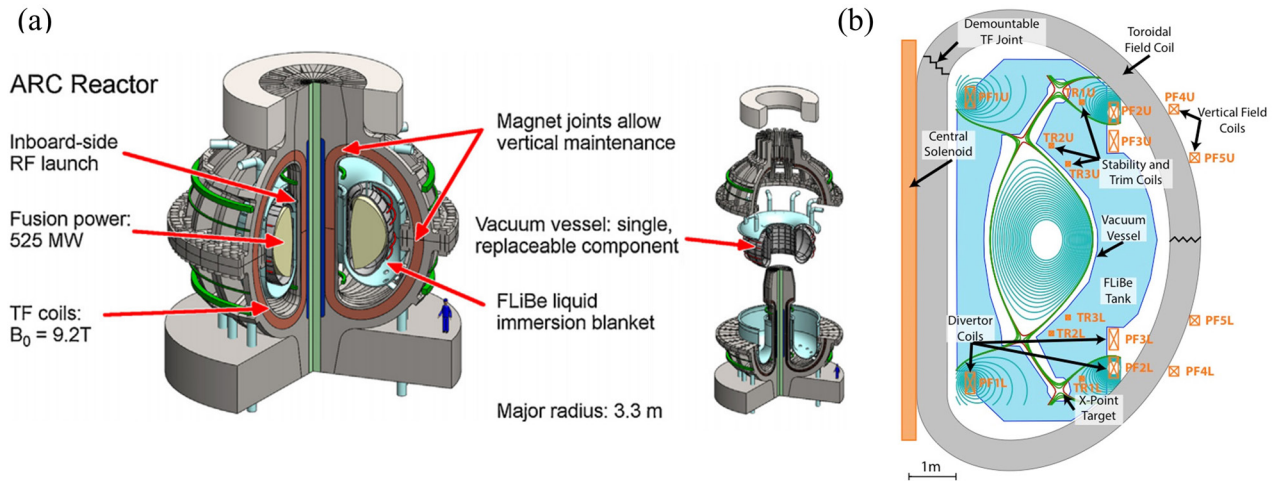


Figure 1. (a) 3D ARC reactor design projection, with demountable toroidal magnetic field coils (reprinted from [20], Copyright (2015), with permission from Elsevier). (b) Schematic diagram of the proposed ARC long-legged X-point target divertor (reprinted from [22], Copyright (2018), with permission from Elsevier) with closed (blue) and open SOL (green) magnetic field lines shown.

impurity seeding. However, we have found that the long-legged divertor geometry provides a number of robust divertor scenarios—stable, fully-detached divertor conditions that can handle the nominal 93 MW exhaust power. For a Super-X divertor, only a modest level of impurity seeding (0.5% neon) is required. With ARC’s proposed X-point target divertor geometry, scenarios exist in which the exhaust power may be accommodated without any impurity seeded at all, obtaining a passively-stable, fully detached divertor state. To our knowledge, this is the first time such a scenario has been identified for a power producing tokamak fusion reactor with a $\lambda_{q||}$ that is consistent with empirical scalings. In order to ensure that the numerical results are robust against model assumptions, sensitivity studies were performed, including: variation of cross-field transport coefficients in the divertor leg, variation of power split between inner and outer divertor legs and variation of separatrix plasma density. This paper presents a snapshot of what has been investigated to date and highlights areas in which further research and refinement of the modelling are needed.

This paper is structured as follows: section 2 describes the UEDGE physics model used for the ARC study; section 3 applies this model to a Super-X divertor setup and presents the results for input power scans both with and without impurity seeding; section 4 presents the results applying the same model and power scans to an X-point target divertor geometry without any impurity seeding. Sensitivity studies performed for various model assumptions and parameters are presented in section 5; Discussion of the results and conclusions are in sections 6 and 7 respectively.

2. UEDGE ARC SOL physics model

UEDGE is a well-established edge fluid simulation code [26–28], which has been extensively used for interpretation of tokamak edge data [29–31] and for modelling of advanced divertors [32]. Most recently, UEDGE has been applied to modelling X-point target divertors in the ADX (Advanced

Divertor eXperiment) concept [25], making it an ideal tool for extending the study of X-point target divertors to ARC.

The ARC design study employed the ACCOME MHD equilibrium solver [33, 34], which allows for a self-consistent computation of magnetic equilibria accounting for non-inductive current drive. The reference magnetic equilibrium used for this study corresponds to the ARC operation design point described in [22], with poloidal coils currents specified in table 1 and power exhaust specified in table 8 of that reference.

ARC employs an upper- and lower-divertor configuration for double-null operation (figure 1(b)). The magnetic equilibrium data from ACCOME were used to implement a lower-half-domain ARC geometry into UEDGE for two divertor setups: (a) Super-X Divertor (SXD), and (b) secondary X-point target divertor (XPTD). Figure 2 shows UEDGE grids generated for each case. Both configurations are considered in these modelling studies to see how they compare with each other for ARC. For exploration of the XPTD magnetic geometry (discussed in section 4), currents in poloidal field coils PF2L and PF2U were varied about the design point value, generating magnetic equilibria with ACCOME that produced UEDGE grids with magnetic separation between main and divertor X-point flux surfaces varying from 1.6 to 0.5 mm, mapped to the outer midplane.

In the UEDGE model for ARC used here, the radial particle transport is specified by a diffusion and convection model, given by the equation:

$$\Gamma_{\perp} = -D\nabla n + v_{\text{conv}}n \quad (1)$$

where Γ_{\perp} is the radial particle flux density, D is the diffusion coefficient and v_{conv} is the convective pinch velocity. This form of combined diffusion and convection velocity for anomalous radial transport has been previously used in UEDGE modelling studies [35]. Radial electron/ion energy transport is simulated by a diffusive model, with a specified diffusion coefficient profile, $\chi_{i,e}$, taking the simplifying assumption that the ion and electron thermal diffusivities are equal.

The ARC operational design point parameters [20] combined with empirical characterizations of transport behavior

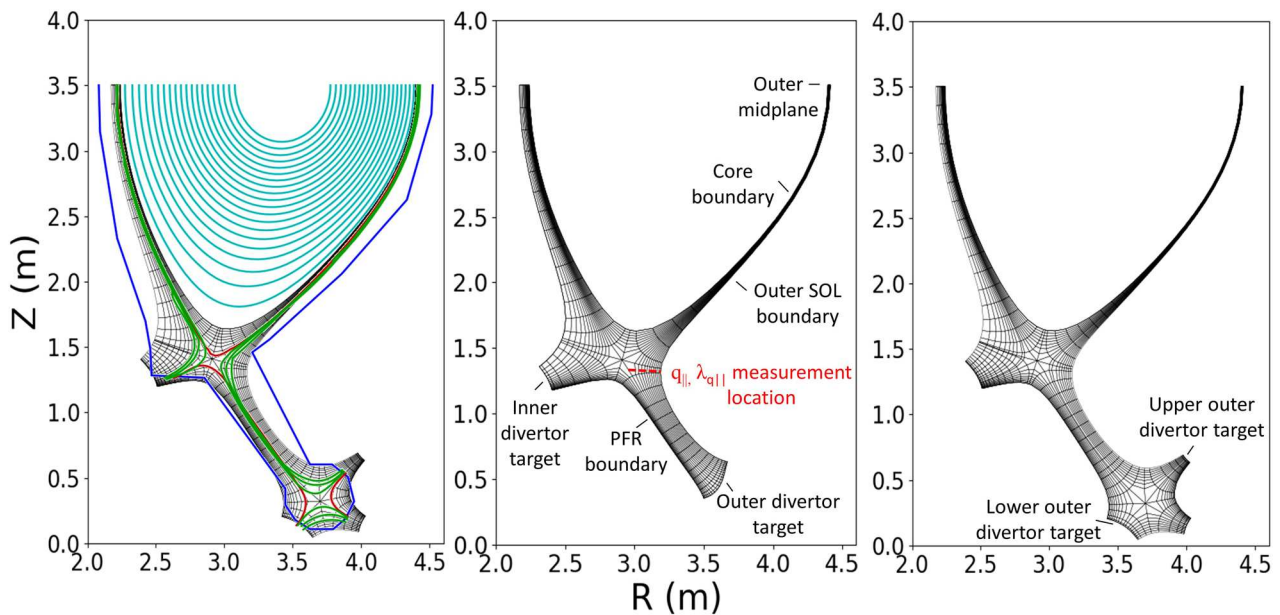


Figure 2. Schematic diagram of UEDGE ARC SOL/divertor grid mapped over magnetic ARC magnetic geometry (left), with the location of the reactor first wall given by the blue line. Plots of simulation grids for the SXD (middle) and XPTD (right) geometries, with labelled simulation boundaries and midplane location shown. The profile parallel heat flux, $q_{||}$, (sum of ion and electron contributions) entering into the divertor and its characteristic e-folding width, $\lambda_{q||}$, is measured at the location of the red dashed line.

in the SOL and divertor were used to determine plausible values for D , v_{conv} and $\chi_{i,e}$. ARC is designed to operate in I-mode [36]—an improved confinement regime with energy confinement comparable to H-mode but with particle confinement similar to L-mode, with a corresponding pedestal in the temperature profiles and lack of a pedestal for the density. The thermal and particle transport models were therefore tuned to produce midplane density and temperature profiles that are representative of I-mode on the basis of what is observed in Alcator C-Mod and plausible for ARC.

The SOL density profile in Alcator C-Mod has been well documented [37, 38] in a variety of regimes—L-Mode, EDA H-Mode, and ELM free H-modes—and certain features like the formation of a density shoulder on the low field side was found to always be present, resulting in a ‘main-chamber recycling’ regime at higher densities [39]. The underlying mechanism is associated with the ballistic motion of interchange-unstable filamentary plasma structures that form in the edge [40]. A large body of experimental evidence accumulated from many tokamaks and other devices [41] indicate that this ubiquitous phenomenon should also appear in ARC. To simulate this situation, the diffusion coefficient D was set to $0.025 \text{ m}^2 \text{ s}^{-1}$ throughout the domain, and a profile for v_{conv} was adjusted to produce a targeted midplane density profile: last-closed-flux surface (LCFS) density at the ARC design value of $n_{\text{LCFS}} \sim 10^{20} \text{ m}^{-3}$, a decay length of $\lambda_n \sim 5.5 \text{ mm}$, and a flattened density profile (‘density shoulder’) at 10 mm radial distance into the SOL (see figures 3 and 4). This SOL density profile and separatrix value are based on I-mode density profile data that has previously been obtained in Alcator C-Mod under high-field operation [36]. Whilst there is substantial uncertainty in assuming these profiles will scale to a reactor like ARC, in the absence of reason to suggest otherwise we assume what has been achieved in Alcator C-Mod

will be attainable in ARC for the purpose of this study. Noting that the core density is at a Greenwald fraction of 0.67, we explore the effect of increasing the separatrix density above this design point value in section 5.1. The assumptions of operating in I-mode, with L-mode-like particle confinement and no pedestal in the core density profile as mentioned above, motivate the ARC separatrix density of 10^{20} m^{-3} , equal to the edge density of the core profiles given in [20]. Based on the sensitivities found, the divertor challenge would be clearly more severe at lower separatrix density, as may be obtained with a H-mode plasma assuming a separatrix density that is 1/3 of the core density [42].

Experimental evidence of plasma blobs in the divertor region [43, 44] indicate that the transport physics of the upstream SOL—interchange dynamics driven by the magnetic curvature and plasma pressure gradient—is also at play in the divertor leg. We therefore apply the v_{conv} profile shown in figure 3 uniformly along the magnetic flux surfaces on the low-field-side (LFS), extending from the outer midplane down to the divertor target plate. The value of D was set to $0.25 \text{ m}^2 \text{ s}^{-1}$ in the outer divertor leg below the main plasma X-point, to allow for a plausible rate of particle diffusion into the private flux region. In section 5, we examine the sensitivity of our model results to a factor of 4 variation in the v_{conv} and D in the outer divertor leg. On the high-field-side (HFS), v_{conv} was set to zero throughout the SOL, as no density shoulder or convective radial flux is observed experimentally on the HFS [45].

We take a base value for the power exhaust crossing the LCFS into the SOL, P_{SOL} , of 105 MW for our ARC model (1/5 fusion power). Ion/electron energy diffusion coefficients of $\chi_{i,e} = 0.1 \text{ m}^2 \text{ s}^{-1}$ are set throughout the domain (typical value for H-mode plasma simulations [47]), with exception of the LCFS region in which a transport barrier (i.e. reduced $\chi_{i,e}$ value) is applied. Note that previous studies have found

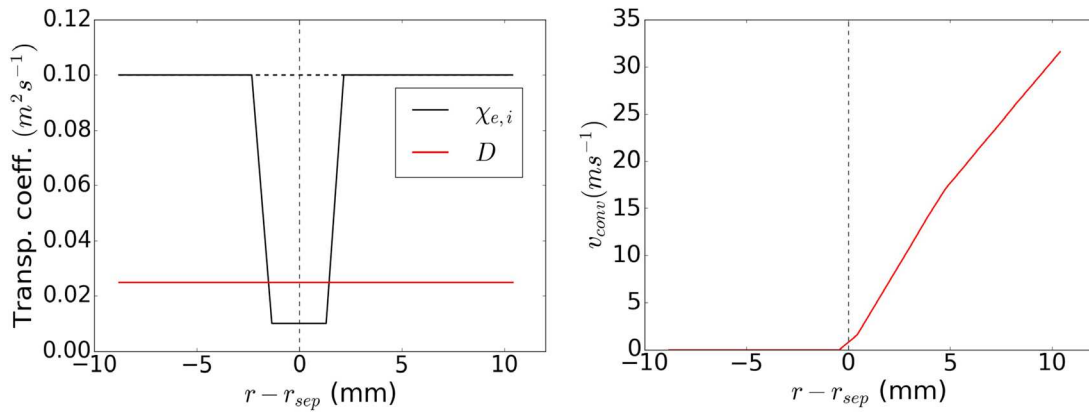


Figure 3. Outer midplane profiles for D , $\chi_{i,e}$ and v_{conv} defined for the UEDGE transport model, plotted as a function of distance from the separatrix into the scrape off layer when mapped to the outer midplane.

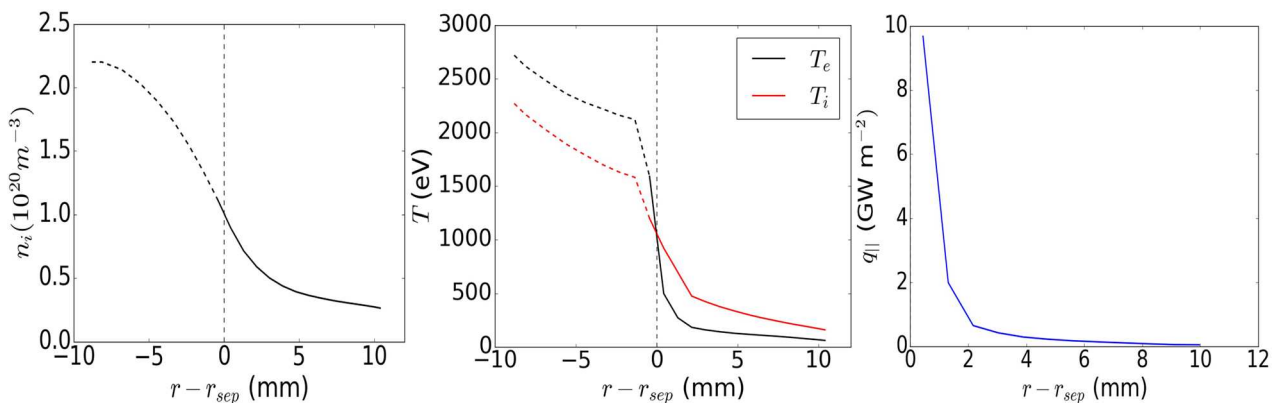


Figure 4. Outer midplane profiles for n , T_e and T_i , as well as $q_{||}$ profile at the primary X-point location (see figure 2), produced for the ARC I-mode model, plotted as a function of distance from the separatrix into the scrape off layer when mapped to the outer midplane. The dashed line sections inside the separatrix do not represent the core profiles postulated in ARC, but instead serve to establish the required boundary conditions at the separatrix. Parameters are shown for a SXD simulation. For this case, the peak value of $q_{||}$ entering into the divertor is approximately 10 GW m^{-2} , with $\lambda_{q_{||}} \sim 0.55 \text{ mm}$.

spatially constant $\chi_{i,e}$ was sufficient to match experimentally observed midplane temperature profiles in C-Mod L-mode plasmas [49], but a transport barrier is required here to achieve the narrow $\lambda_{q_{||}}$ anticipated and to reproduce the shape of observed H/I-mode SOL temperature profiles. Based on the Eich empirical scaling law [23] and a recent extension of the heat flux width database to include I-mode plasmas [46], we anticipate that the heat flux width in ARC at its operational design point will be $\lambda_{q_{||}} \sim 0.4 \text{ mm}$. To attempt to create this value, an energy transport barrier is created $\sim 1 \text{ mm}$ on either side of the separatrix on the low-field side (LFS) of the confined plasma by decreasing $\chi_{i,e}$ to $0.01 \text{ m}^2 \text{ s}^{-1}$ (note though that as LCFS grid resolution changes across various SXD/XPTD grids implemented, this value requires adjusting—see sections 3 and 4). The parallel heat flux profile $q_{||}$ (i.e. the sum of electron and ion heat flux densities) across the entrance to the divertor leg is measured to verify the e-folding width of 0.4 mm when mapped to the outer midplane (see measurement location as the dashed line in figure 2 and resultant profile in figure 4). On the high-field side (HFS), the transport barrier was enhanced by decreasing $\chi_{i,e}$ further to $0.005 \text{ m}^2 \text{ s}^{-1}$. This creates an approximate 10:90 split of exhaust power across

the separatrix to the HFS:LFS, consistent with observations from near-double-null I-mode plasmas on C-Mod [9] as well as MAST double-null operation [50]. This energy transport barrier in $\chi_{i,e}$ is only applied at the interface between open and closed magnetic flux surfaces in the main-chamber region, and not in the divertor legs.

A reproduction of plasma profiles in ARC's core and pedestal regions is not attempted for this study of the SOL and divertor, and dashed line sections of the midplane profiles (figure 4) inside the separatrix do not represent the core profiles postulated for ARC in [20]. These instead serve to establish the required boundary conditions at the separatrix mentioned for the SOL profiles above. Density at the core plasma boundary is set to obtain a fixed density at the separatrix of nominally $1 \times 10^{20} \text{ m}^{-3}$. Equal electron and ion powers entering the domain are also specified at the core plasma boundary to obtain the total desired power crossing the LCFS (where total power in these half-domain simulations is taken as half of the total exhaust power entering the SOL in the full ARC domain, P_{SOL}). Neumann boundary conditions are applied to the edge/private flux region (PFR) boundaries in the form of radial linear extrapolations to the guard cells for both

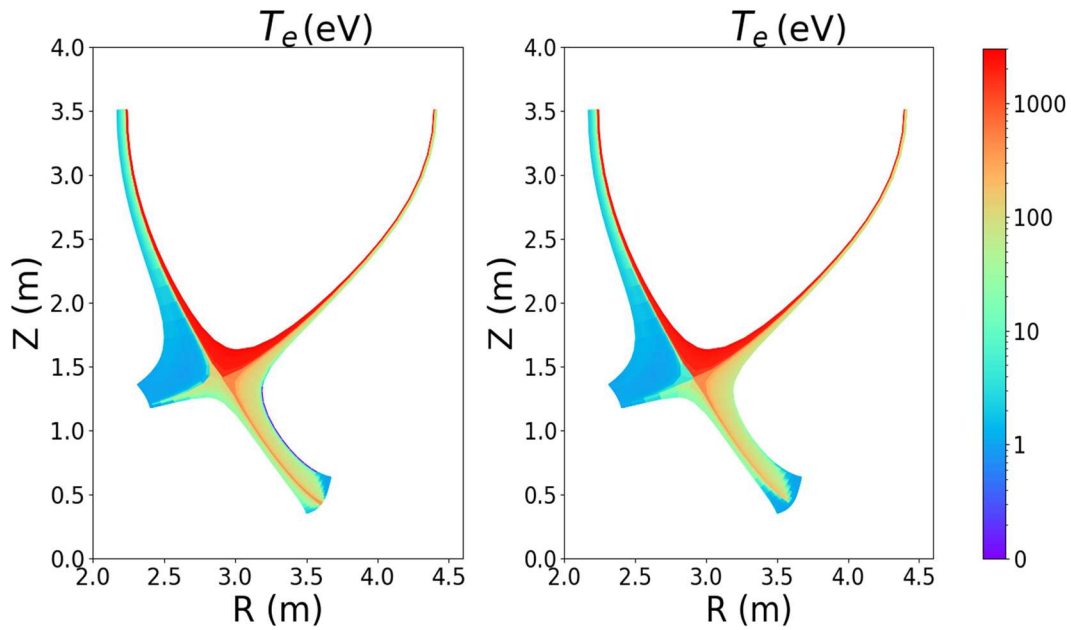


Figure 5. 2D T_e plots for ARC SXD steady-state solutions, for $P_{\text{SOL}} = 105$ MW both without impurity seeding (left) and with 0.5% neon impurity fraction (right).

plasma density and for electron/ion temperature. It is worth noting that the edge boundary in this case represented a region in the far SOL, rather than a first wall boundary, since the simulation grid did not reach the reactor first wall (see figure 2). Target plates employ a plasma sheath boundary condition. Neutral recycling was set to 100% at both target and edge/PFR boundaries (to achieve particle balance in the simulation domain for steady-state operation [51]), with neutrals being included in the UEDGE diffusive model [29]. To simulate just a lower-half domain for ARC, we assume up-down symmetry in the divertor response, and as such a symmetry condition was implemented at the poloidal midplane boundaries. This required performing the UEDGE simulations without particle drifts; drift effects introduce up-down asymmetries that would be incompatible with such a symmetry condition. Using the described model, UEDGE was run to produce converged steady-state solutions for all results shown in this paper.

3. ARC Super-X divertor

3.1. Without impurity seeding

This physics model is initially applied to the SXD geometry for the ARC ‘base-case’, i.e. a DT plasma with 105 MW of exhaust power crossing the LCFS into the SOL and with no impurity seeding to enhance radiation in the divertor. Results assuming a pure deuterium plasma have previously been reported in [52]. A 2D T_e plot is given in figure 5 for the converged UEDGE solution for the ARC base-case. The transport barrier in $\chi_{i,e}$ produced a parallel power decay width $\lambda_{q\parallel}$ of ~ 0.55 mm (marginally greater than 0.4 mm desired, but limited by the LCFS resolution that could be attained for viable SXD grids generated in UEDGE), resulting in a narrow high temperature, high power flux intensity region in the near SOL outside the separatrix, that extends down to the divertor

plate. The peak q_{\parallel} at the X-point entering the divertor region was measured to be ~ 10 GW m^{-2} (see figure 4). Peak electron temperature at the outer target plate for this base case are in excess of 300 eV (whilst the inner target remains detached), far above what target materials could be expected to survive.

In practice, core radiation may result in the exhaust power entering the SOL from the core being less than the 105 MW assumed in this case (i.e. 93 MW for the ARC operational design point value). Keeping all other parameters/conditions fixed, a power scan was performed by steadily reducing P_{SOL} , to determine the power window for which stable detachment could be obtained. The results are shown in figure 6(a). Stable detached solutions (where plate $T_e < 1$ eV) are obtained for the power window of 32–40 MW. Below 32 MW, the solution develops an ‘X-point MARFE’—the detachment front moves up the entire divertor leg and into the core plasma.

3.2. With 0.5% neon impurity seeding

To improve the power handling performance of the ARC SXD setup, a 0.5% neon (Ne) impurity was introduced in the ‘fixed fraction’ model—where impurity concentration is set at a percentage of the plasma electron density throughout the domain—to increase radiation energy losses of the plasma in the SOL. A power scan was repeated, the results of which are shown in figure 6(b). The results produced a bifurcation in solutions with two branches: a hot and a cold branch. The cold branch is accessible by ramping up input power and neon impurity fraction in tandem from an initially detached solution, in order to maintain detachment until 0.5% Ne fraction is obtained. This branch shows detachment can be obtained at much higher P_{SOL} with the presence of the Ne impurity, now with a P_{SOL} window of 80–108 MW. Below 80 MW, the cold branch solutions develop an X-point MARFE. Increasing P_{SOL} above 108 MW results in transition to the hot branch,

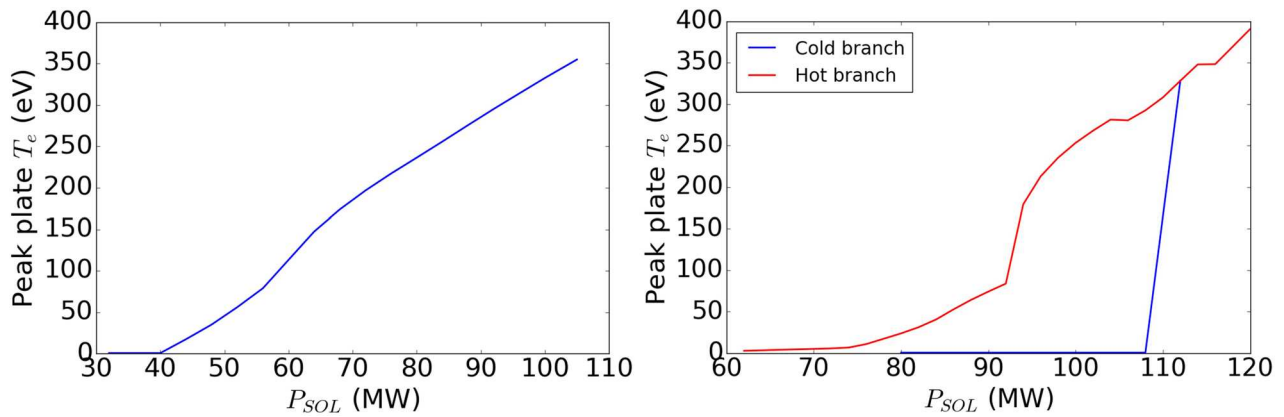


Figure 6. SXD power scan results showing peak outer plate T_e (eV) against exhaust power P_{SOL} (MW) for 0% neon fraction (left) and 0.5% neon fraction (right).

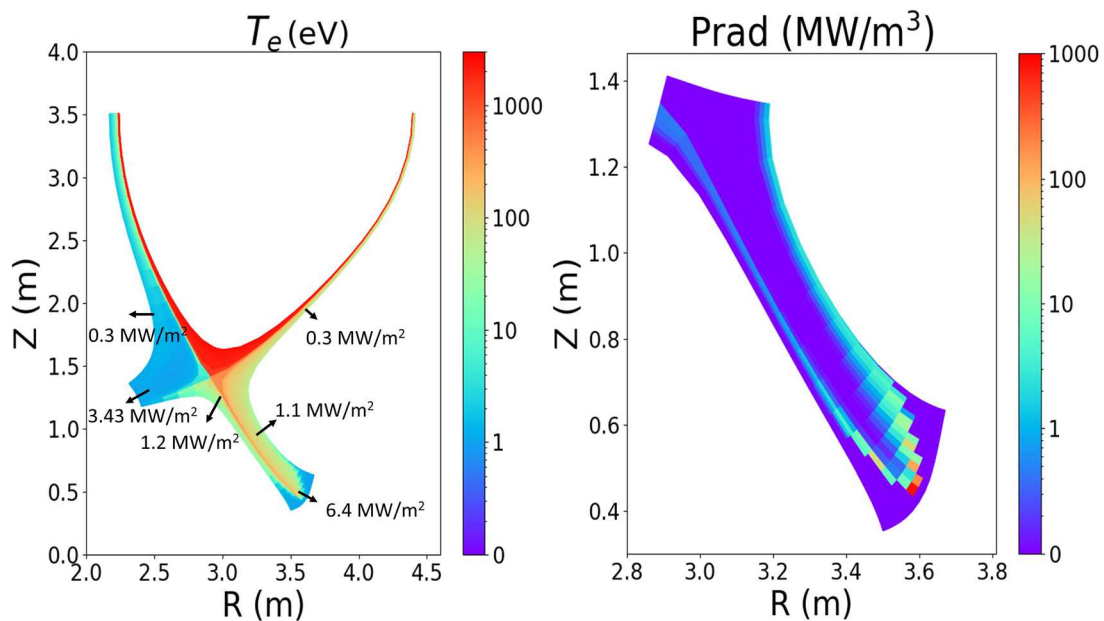


Figure 7. 2D plots for $P_{SOL} = 105$ MW, 0.5% Ne impurity detached SXD solution of (left) T_e with annotated peak power flux densities to the boundaries, for combined plasma and radiation power loadings, and (right) neon impurity radiation emissivity, with a peak value of 855 MW m^{-3} .

after which a reduction in P_{SOL} does not result in a transition back to a detached solution, but plate temperatures remain hot until $P_{SOL} < 62$ MW where the hot branch solutions MARFE. Such bifurcations have previously been observed in UEDGE solutions [29], and have also been studied analytically [53].

A plot of T_e for a detached case (with $P_{SOL} = 105$ MW) is shown in the right-hand plot in figure 5. The same narrow, high temperature region is observed in the temperature profile, but now with distinct regions dropping to $T_e < 1$ eV for both the inner and outer target plates. Figure 7 shows the same plot with annotation of the peak power flux densities to different boundaries, from combined plasma and radiation power loadings. The peak power flux density measured was 6.4 MW m^{-2} to the outer target plate, lower than the 10 MW m^{-2} accepted as the maximum power flux that can be accommodated by a solid wall. This is despite the presence of a high-intensity Ne radiation front directly above the target plate (figure 7 (right)), with a peak emissivity of 855 MW m^{-3} .

4. ARC X-point target divertor

The same physics model described in section 2 was applied to the XPTD geometry. Several XPTD grids were implemented in UEDGE with different primary and divertor X-point radial separations, ranging from 1.6 mm to 0.50 mm (mapped to outer midplane). The grids generated consistently have two radial grid cells separating the two X-point separatrices, and hence reducing the radial X-point separations corresponds to increasing the resolution around the LCFS. Anticipating a decrease in $\lambda_{q||}$ with increasing resolution at the LCFS (since the previous SXD model was resolution limited to $\lambda_{q||} \sim 0.55$ mm), the depth of the transport barrier was adjusted on the LFS to $\chi_{i,e} = 0.02 \text{ m}^2 \text{ s}^{-1}$. Scans of P_{SOL} are repeated for the various XPTD grids without any Ne impurity seeding, and results are plotted alongside the SXD power scan results for comparison (figure 8). Power scans are performed for both decreasing P_{SOL} from the attached 105 MW base scenario (a

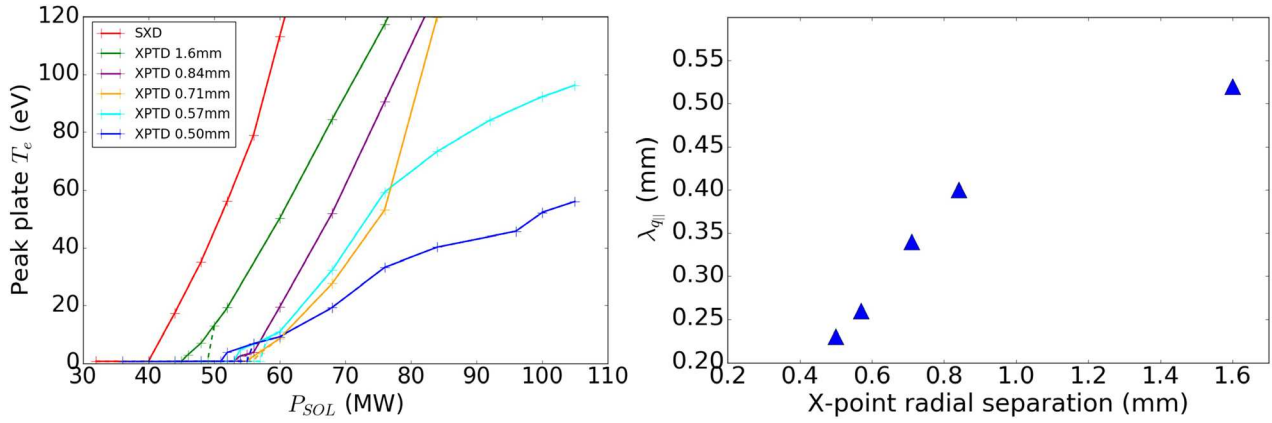


Figure 8. (Left) Peak outer target T_e versus exhaust power P_{SOL} , for SXD and XPTD grids with radial X-point separations ranging from 1.6 mm to 0.50 mm. ‘Downswing’ power scan solutions are shown with solid line and ‘upswing’ scans by the dashed lines. (Right) Measured $\lambda_{q||}$ against X-point radial separation for XPTD cases with fixed $\chi_{i,e}$ transport model. The SXD case had $\lambda_{q||} \sim 0.55$ mm.

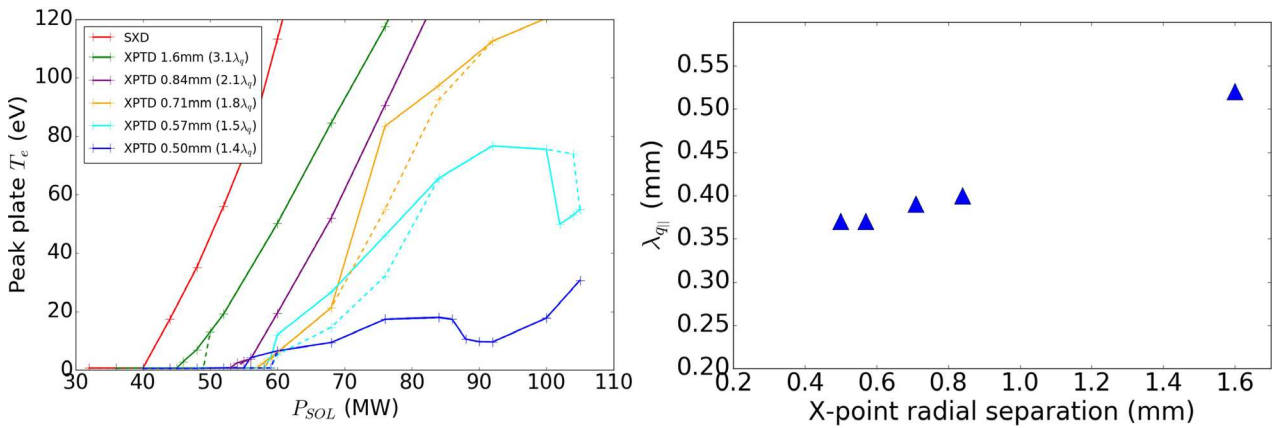


Figure 9. (Left) Peak outer target T_e versus exhaust power P_{SOL} for repeated downswing (solid line) and upswing (dashed line) power scans for SXD and XPTD grids with adjusted $\chi_{i,e}$ transport model to maintain $\lambda_{q||} \sim 0.4$ mm. (Right) New measured $\lambda_{q||}$ across XPTD grids with adjusted $\chi_{i,e}$ transport model.

‘downswing’ power scan) and for increasing P_{SOL} from a low-power, detached state (an ‘upswing’ scan). Peak $q_{||}$ at the primary X-point increases from ~ 9 to 15 GW m^{-2} across XPTD grids with narrowing X-point spacing and corresponding increasing resolution at the LCFS. A $\sim 30\%$ – 40% increase in $\lambda_{q||}$ is observed over a power scan for the fixed transport model at the transition to the detached divertor regime across all grids. Such $\lambda_{q||}$ broadening under detached divertor conditions has been observed in experimental studies [54].

The results show slight gains in detachment threshold for the XPTD geometries over the SXD, however, values of $q_{||}$ and $\lambda_{q||}$ were not maintained fixed as described further below. The 1.6 mm X-point separation grid increases the detachment threshold for the downswing power scan (solid line) from $P_{SOL} = 40$ to 46 MW, and then for smaller X-point separations in the range of 0.84–0.50 mm, detachment threshold cluster in the range of $P_{SOL} = 52$ – 56 MW. The upswing power scans (dashed lines) show similar results, but with detachment threshold 2–4 MW greater than for the downswing scans. Analysing $\lambda_{q||}$ over XPTD grids shows that as the X-point radial separation gets smaller and resolution around the LCFS increases, the measured value of $\lambda_{q||}$ is found to be decreasing (figure 8). This indicates that our results are still resolution

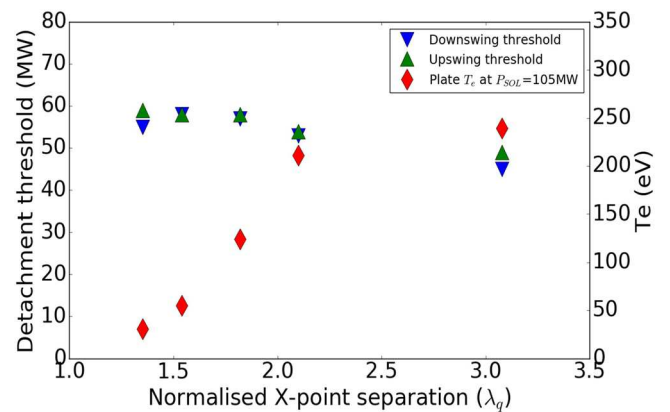


Figure 10. Plots of downswing/upswing power scan detachment thresholds (MW) and peak plate T_e (eV) at $P_{SOL} = 105$ MW against XPTD X-point separation (normalised to $\lambda_{q||}$).

limited for the current transport model. For the grids with the narrowest separations of 0.71, 0.57 and 0.50 mm, $\lambda_{q||}$ drops below the 0.4 mm Eich-scaling width anticipated for ARC, dropping as low as 0.23 mm.

In an attempt to hold $\lambda_{q||}$ fixed at 0.4 mm, the downswing and upswing power scans were repeated with the $\chi_{i,e}$ transport

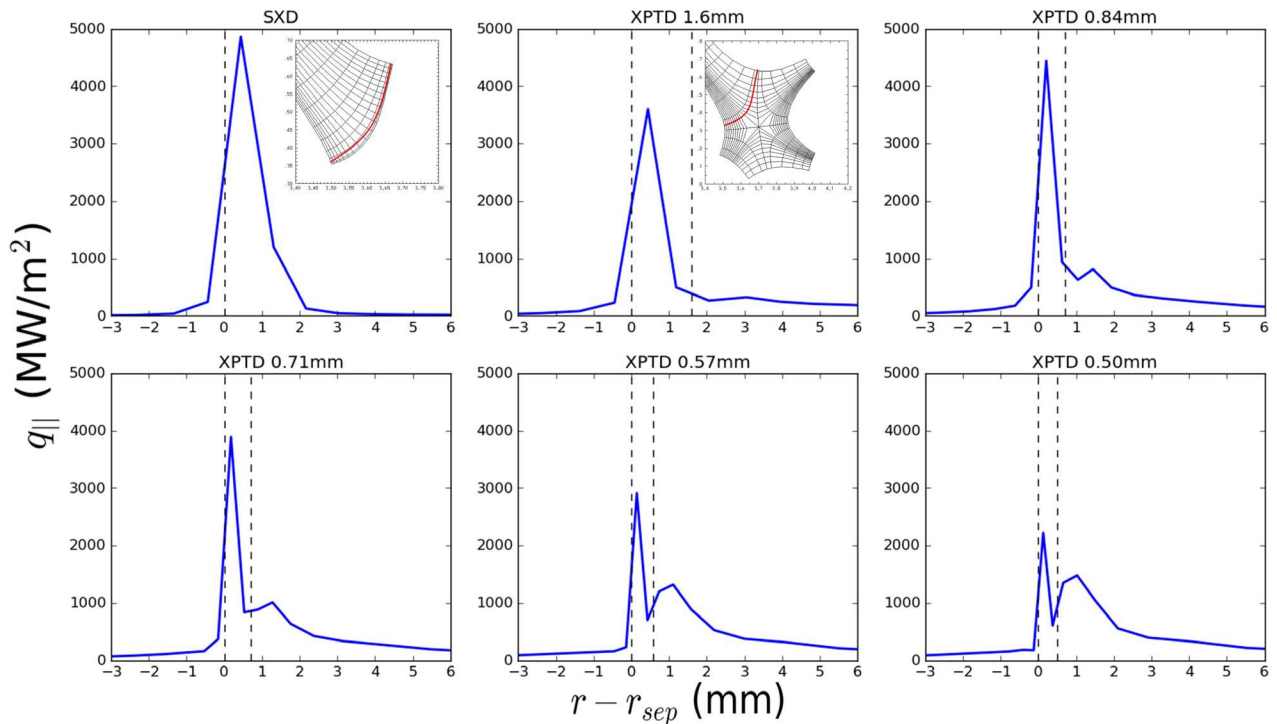


Figure 11. Plots of $q_{||}$ measured above the divertor target for the SXD and above the divertor X-point for the XPTD grids, mapped to the midplane. Separatrices locations shown with dashed lines. Inset plots in frames 1 and 2 show location of measured $q_{||}$ for the SXD and XPTD grids respectively.

barrier depth adjusted for the 0.71, 0.57 and 0.50 mm separation XPTD grids to 0.035, 0.065 and 0.085 $\text{m}^2 \text{s}^{-1}$ respectively on the LFS (as well as 0.007, 0.007 and 0.008 $\text{m}^2 \text{s}^{-1}$ respectively on the HFS to maintain the 10:90 HFS:LFS power split). Power scan results are plotted in figure 9 alongside the new measured $\lambda_{q_{||}}$ values. Detachment thresholds and the peak plate temperatures at the P_{SOL} base value of 105 MW grids are plotted for all grids in figure 10. Now maintaining near-constant $\lambda_{q_{||}}$ across 0.84–0.50 mm separation grids, the normalised X-point separation in $\lambda_{q_{||}}$ steadily decreases across XPTD grids, spanning a range of 3.1–1.4 $\lambda_{q_{||}}$.

For the two grids with the smallest X-point separations of 0.57 and 0.50 mm, an unexpected behavior is observed: as P_{SOL} is increased, sharp decreases in plate temperature occur at certain P_{SOL} values. These appear to represent transitions across different branches of solutions, akin to the ‘hot’ and ‘cold’ branch solutions observed for the SXD Ne impurity seeded cases shown in section 3.2, but over much smaller power windows. (It is noteworthy that for these impurity-free solutions, large detachment power threshold hysteresis loops, as seen in section 3.2, are not present here.) One possible explanation is that as the target X-point is becoming more engaged in attenuating and splitting the power flux (i.e. spacing less than $2\lambda_{q_{||}}$) non-linearities associated with the power loss channels of hydrogenic radiation and plasma-neutral interactions play a more important role. Further study of this behaviour was beyond the scope of the present investigation and should be pursued.

Apart from an initial gain from decreasing X-point spacing from 1.6 to 0.84 mm, detachment threshold remains fairly constant in the ranges of 53–58 MW and 54–59 MW for

downswing and upswing power scans respectively for all grids with X-point separations smaller than 0.84 mm. The gain in threshold over the SXD (detaching at $P_{\text{SOL}} = 40$ MW) is significantly less than previously observed in modelling for the geometries in ADX, which found a factor of ~ 2 gain in threshold for the XPTD over the SXD [25]. However, the ADX study employed an X-point spacing of $0.7 \lambda_{q_{||}}$, which we have not yet explored. Indeed, reducing X-point separation does result in a steadily decreasing peak target plate temperature at the base case $P_{\text{SOL}} = 105$ MW, decreasing by nearly a factor of 10 by the 0.50 mm XPTD grid from 240 to 31 eV (figure 10). Why this does not result in higher detachment thresholds is not yet understood—the gradient of the plate temperature over a power scan is much shallower for the smaller X-point separations, even accounting for the unusual plate T_e behaviour over these power scans. Additional study is required to identify root causes. Extrapolating the trend in target plate T_e suggests that detachment at the $P_{\text{SOL}} = 105$ MW base value may potentially be achieved with X-point spacing of $\sim 1 \lambda_{q_{||}}$ or less. It is not currently possible to generate grids with spacing lower than 0.50 mm at this time, and this remains an area for further study.

The radial $q_{||}$ profile is analysed for each SXD and XPTD grid in figure 11, for $q_{||}$ above the target plate for the SXD and above the divertor X-point for the XPTD cases. Relating to $\lambda_{q_{||}}$, all cases have radial X-point separations greater than $1 \lambda_{q_{||}}$, and so the majority of the exhaust power is directed to the lower target in the outer XPTD leg (which is subsequently referred to as the ‘primary target’). For separations of several $\lambda_{q_{||}}$, very little exhaust power is split from the main heat flux channel towards the upper target in the X-point

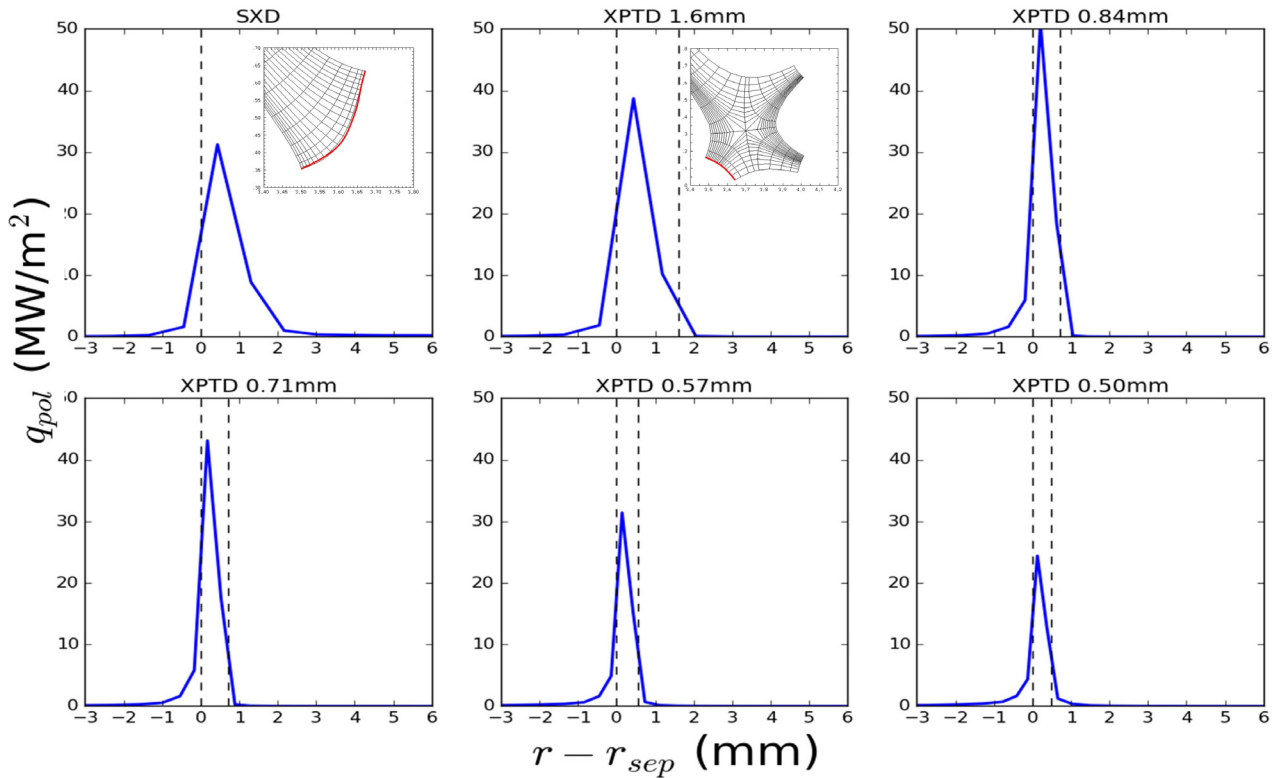


Figure 12. Plots of q_{pol} measured above the divertor target plate for the SXD and XPTD grids, mapped to the midplane. Separatrices locations shown with dashed lines. Inset plots in frames 1 and 2 show location of measured q_{pol} for the SXD and XPTD grids respectively.

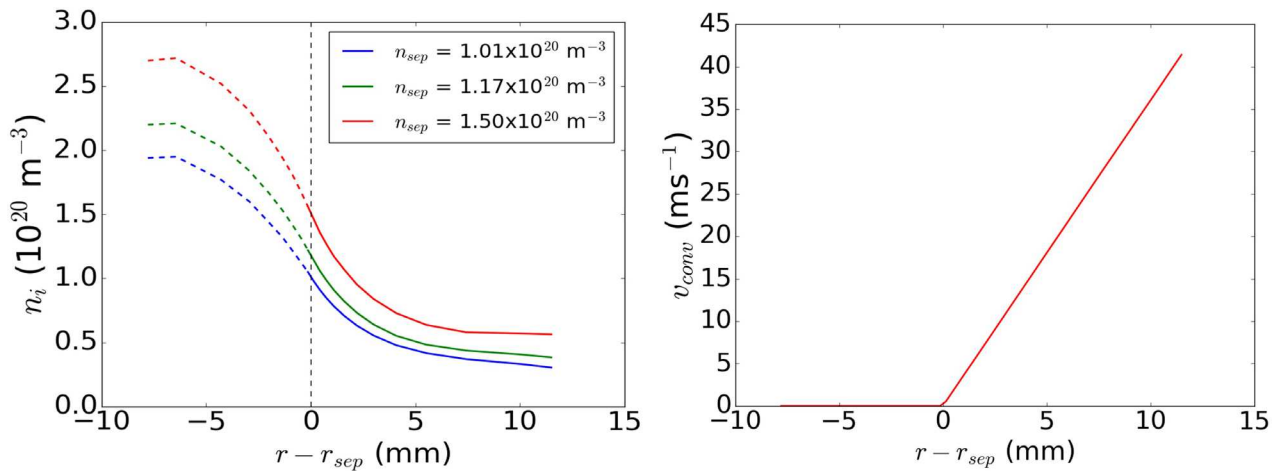


Figure 13. Plots of midplane density profiles for the three n_{sep} cases investigated (left) and the new v_{conv} profile for the $1.50 \times 10^{20} \text{ m}^{-3}$ case (right).

region, and hence the divertor behaves in a similar manner to the SXD setup. When X-point separations are smaller, a larger fraction of the total exhaust power is split from the main heat flux channel, and the peak $q_{||}$ profile significantly reduces. This is at least consistent with the drop in target plate temperature for narrowing X-point spacing. To reduce the peak $q_{||}$ further, normalised X-point separations of $\sim 1 \lambda_{q||}$ or lower may be required to properly engage the divertor X-point for enhanced power handling performance. This provides further motivation to study XPTD grids with $1 \lambda_{q||}$ separations or lower.

The poloidal power flux, q_{pol} , is calculated for each case and shown in figure 12. These data indicate that by reducing the X-point spacing to $1.4 \lambda_{q||}$ the peak plasma power loading on the primary target is reduced from a maximum of $\sim 50 \text{ MW m}^{-2}$ to $\sim 25 \text{ MW m}^{-2}$. This result is encouraging; with target plate tilting (not employed in this design) peak power loading may be reduced to less than $\sim 10 \text{ MW m}^{-2}$, which is remarkable considering the peak parallel heat flux entering the divertor of $\sim 10 \text{ GW m}^{-2}$ and the lack of impurity radiation in these divertor scenarios.

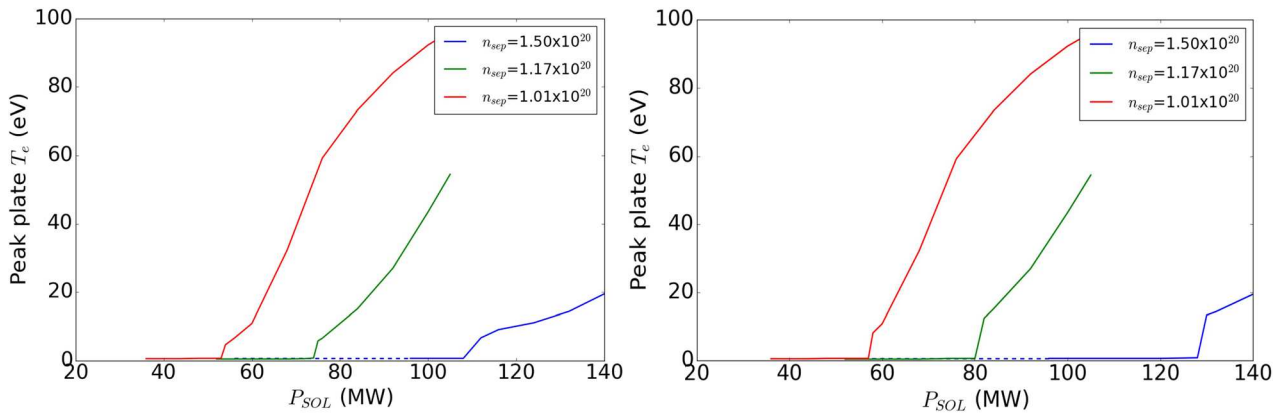


Figure 14. Plots of downswing (left) and upswing (right) powerscan results for peak plate temperature (T_e) for the ARC base upstream separatrix density $1.01 \times 10^{20} \text{ m}^{-3}$ and the increased $1.17 \times 10^{20} \text{ m}^{-3}$ and $1.50 \times 10^{20} \text{ m}^{-3}$ cases for the 0.57 mm X-point separation grid, corresponding to a normalized X-point separation of $2 \lambda_{q||}$. The dashed blue line indicates unconverged solutions with the detachment window for the $n_{\text{sep}} = 1.50 \times 10^{20} \text{ m}^{-3}$ case.

5. Model sensitivity studies for the XPTD

A number of assumptions are made in the modelling, some of which are not experimentally validated as of yet—in particular assumptions in relation to the upstream separatrix density and the radial transport along the divertor leg. In this section, various model parameters relating to these assumptions are varied, to test the robustness and sensitivity of our ARC model solutions.

5.1. Upstream density

The ARC design point reference discharge [20] used for this study, with separatrix density of $\sim 1 \times 10^{20} \text{ m}^{-3}$, has Greenwald density fraction of 0.67. Thus it may be possible to operate ARC at a higher plasma density, further increasing the power range over which an impurity-free detached divertor regime may be obtained. In order to examine this, the upstream separatrix density was increased from the reference point value of $1.0 \times 10^{20} \text{ m}^{-3}$ to $1.2 \times 10^{20} \text{ m}^{-3}$ and $1.5 \times 10^{20} \text{ m}^{-3}$, by adjusting the core density boundary condition. This was performed for the 0.57 mm separation XPTD grid with the $\chi_{i,e}$ transport barrier model described at the start of section 4 (transport barrier depth of $\chi_{i,e} = 0.02 \text{ m}^2 \text{ s}^{-1}$ and $0.005 \text{ m}^2 \text{ s}^{-1}$ for LFS and HFS respectively), having a normalized X-point spacing of $2 \lambda_{q||}$. For the $1.5 \times 10^{20} \text{ m}^{-3}$ case studies, re-tuning of the v_{conv} profile was required to retain a similar midplane density profile properties as for the lower density cases (i.e. decay length of $\lambda_n \sim 5.5 \text{ mm}$, flattened density shoulder in far SOL). The new v_{conv} and midplane n profiles are shown in figure 13.

Downswing and upswing powerscans were repeated for the new cases with the 0.57 mm X-point separation grid, and results for these are plotted alongside the ARC base scenario ($1 \times 10^{20} \text{ m}^{-3}$) in figure 14. A significant increase in detachment threshold is observed in both power scan directions, increasing from 53 to 108 MW for the downswing power scan, and from 57 to 128 MW for the upswing power scan. The difference between downswing/upswing detachment thresholds has substantially widened under these higher

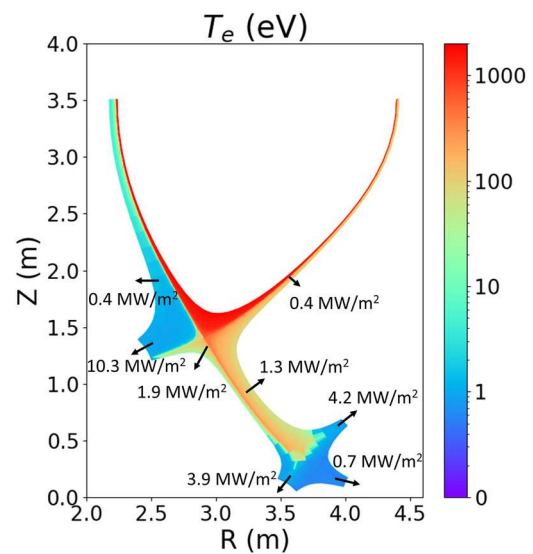


Figure 15. Peak power flux densities to domain boundaries for the detached $P_{\text{SOL}} = 105 \text{ MW}$, $n_{\text{sep}} = 1.50 \times 10^{20} \text{ m}^{-3}$ solution.

density conditions. At $n_{\text{sep}} = 1.5 \times 10^{20} \text{ m}^{-3}$, the solutions obtained fully handles the ARC exhaust power in both power scan directions, without any use of impurity seeding.

Converged solutions below $P_{\text{SOL}} = 96 \text{ MW}$ could not be obtained for this ARC model with raised upstream density. However, in the range of $P_{\text{SOL}} = 56\text{--}96 \text{ MW}$, despite solutions failing to converge the detachment front remains near-stationary within the divertor leg volume for a given P_{SOL} value, with X-point MARFE onset only occurring when $P_{\text{SOL}} < 56 \text{ MW}$. The dashed line on figure 14 marks these unconverged solutions. This makes the full extent of detachment window in this case poorly defined (whilst detachment threshold remains well defined still), but likely to still contain the 93 MW ARC design point power exhaust within this window. Peak power fluxes to the boundaries for the detached $P_{\text{SOL}} = 105 \text{ MW}$ solution are calculated and shown in figure 15, showing acceptable power flux densities to all boundaries (with the inner divertor target being on the $\sim 10 \text{ MW m}^{-2}$ limit, but could be reduced by introducing target plate tilting).

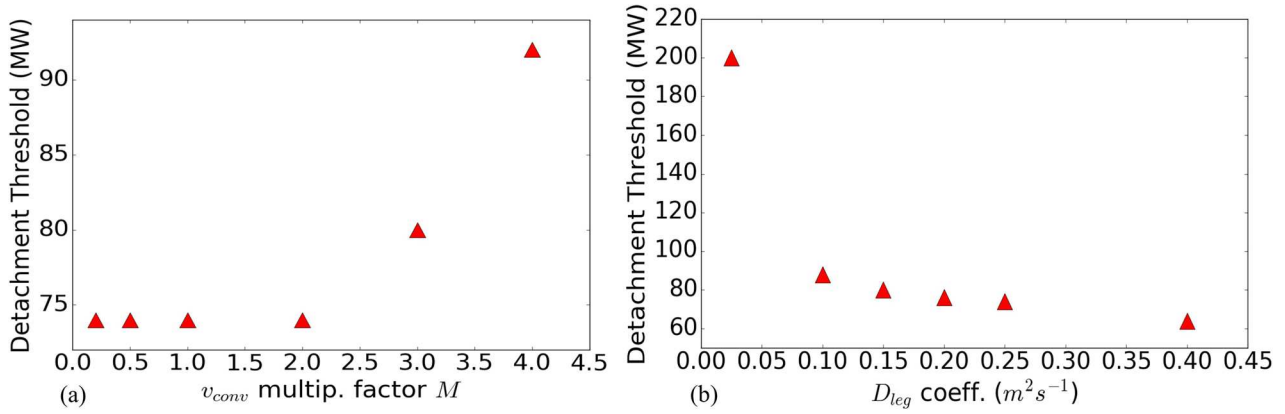


Figure 16. Variation in downswing power scan detachment threshold for variation in outer divertor leg values of (a) v_{conv} multiplier factor M and (b) diffusive transport coefficient D .

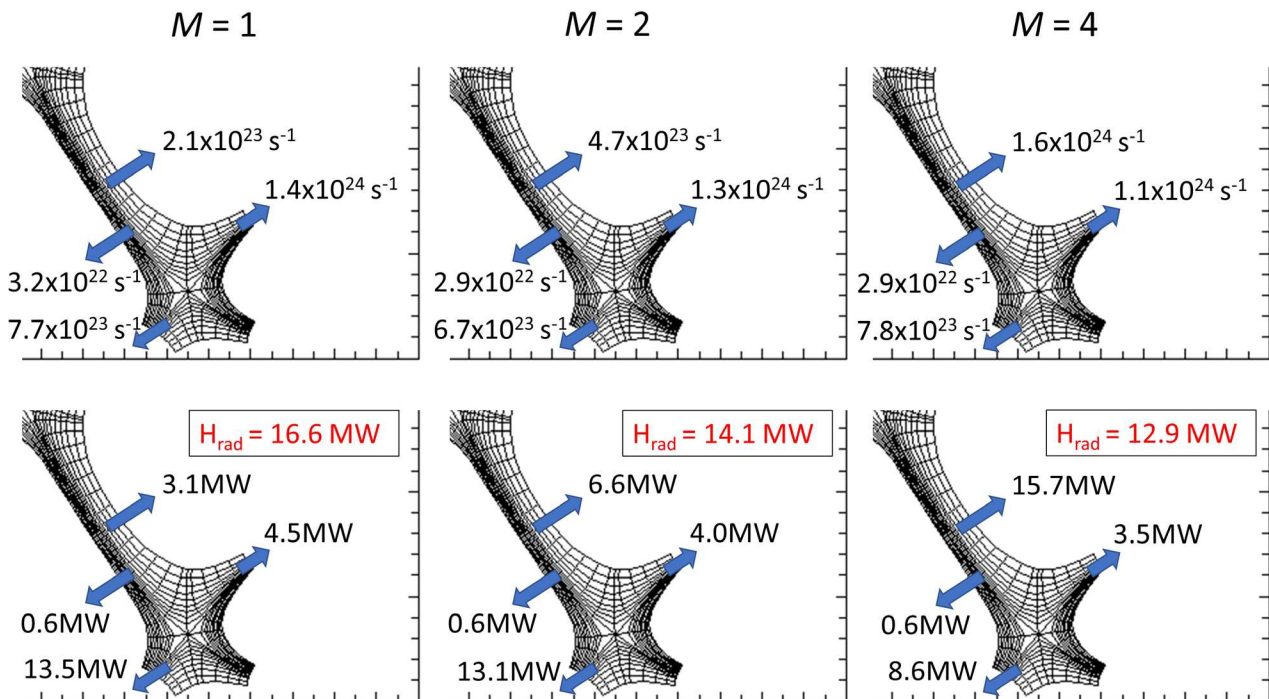


Figure 17. Annotated plots of particle (upper) and plasma power flows (lower) to the divertor leg mesh boundaries for v_{conv} multiplier factors of $M = 1, 2$ and 4 . An estimate of power losses to hydrogenic radiation in the divertor volume is given.

5.2. Leg radial transport coefficients D and v_{conv}

The magnitude of the radial transport in the long outer divertor leg is one assumption in our model without experimental validation, in particular, lacking experimental data on tightly-baffled, long-legged divertor behaviour. To assess the effect of relaxing this assumption, the magnitude of the transport coefficients D and v_{conv} in the divertor leg volume are varied to assess sensitivity to radial transport for our solutions.

The magnitude of the convection velocity was changed by multiplying the base-case v_{conv} profile given in figure 3 by a multiplication factor M , such that $v_{conv}^{new} = M v_{conv}^{orig}$, in the outer divertor leg volume only. A ‘downswing’ powerscan was performed again with the 0.57 mm separation XPTD grid, $n_{sep} = 1.2 \times 10^{20} m^{-3}$ case from section 5.1 for each value of M studied, with all other factors held constant, to find the new detachment threshold. Results are plotted in figure 16(a).

For multiplication factors between 0.2 and 2 the detachment threshold is unchanged from the base-case value of 74 MW, and for $M > 2$ the threshold increases. From this we can conclude that our results are robust to variation in v_{conv} magnitude over a reasonable range, with no deterioration in performance and getting only better performance if significantly larger convective transport than assumed is observed.

To interpret these results, particle and plasma power flows to the boundaries are calculated in the divertor leg for each value of M . Annotated plots of these with the divertor leg mesh are given for $M = 1, 2$ and 4 in figure 17. An estimate of power losses to hydrogenic radiation is shown also. These show that, as M is increased from $M = 1$ to 2, despite an increase in the particle flux to the outer SOL the plasma power to the primary target remains similar. Only for $M = 4$ does the power to the primary target drop significantly, and power flow to the outer SOL boundary dominates. It is notable

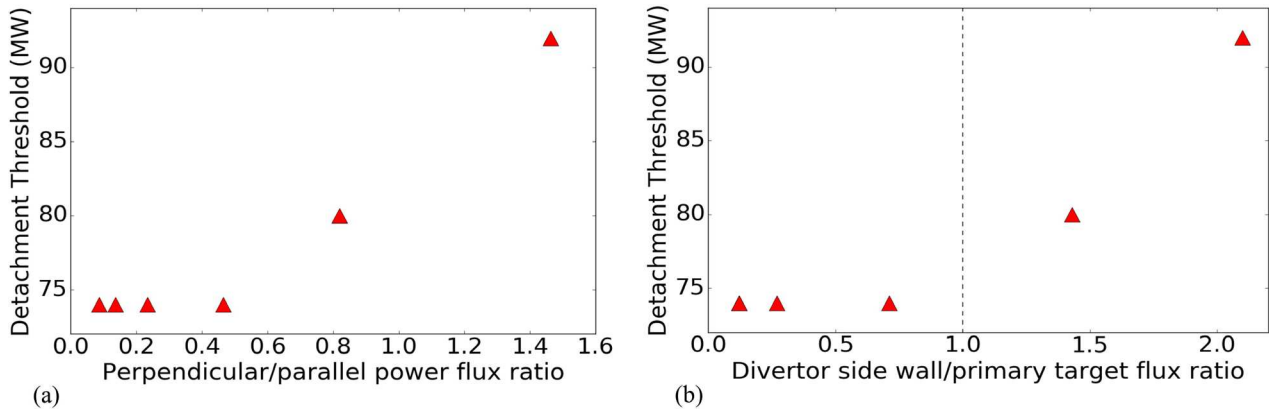


Figure 18. Plots of the calculated ratio of (a) perpendicular/parallel plasma power in the divertor leg, and (b) of side wall/primary target particle flux obtained during a scan of v_{conv} multiplier factors, M .

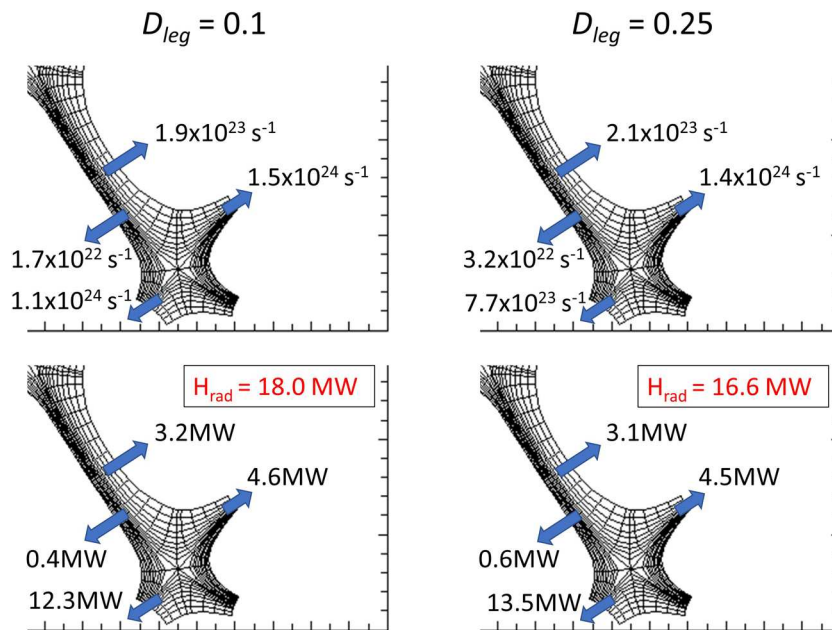


Figure 19. Annotated plots of particle (upper) and plasma power flows (lower) to the divertor leg mesh boundaries for D_{leg} values of 0.1 and $0.25 \text{ m}^2 \text{ s}^{-1}$. An estimate of power losses to hydrogenic radiation in the divertor volume is given.

that this $M = 4$ case is the only one of the three where the particle flux to the outer wall is of the same order of magnitude as the parallel flux to the plates, and exceeding the flux to primary target. In this case we can argue the exhaust power is now directed primarily towards the sidewall, and detachment physics is now more dependent on interaction with the side wall than with the target plate.

To characterise this change, a plot of the calculated ratio of perpendicular/parallel plasma power in the divertor leg is shown in figures 18(a) and (b) shows instead the ratio of side wall/primary target particle flux. Here perpendicular refers to the sum of fluxes arriving along the outer side wall and PFR boundaries, while parallel refers to fluxes arriving at the two target plates. (Note that the outer side wall particle fluxes are not connected to the primary target particle flux via recycling). In figure 18(b) we see a change in detachment threshold response when the ratio of particle fluxes is greater than 1 (whereas no obvious characteristic regime-change value can be identified for the power flux ratio in figure 18(a)).

A transition between two regimes can be characterised as such: when particle flux to the primary target plate exceeds that to the side wall, the power exhaust is dominated by interaction with the target plate and detachment threshold is insensitive to variation in the radial convection velocity within a certain magnitude. When the ratio is greater than 1, power is primarily transferred to the side wall and detachment physics becomes dependent on the plasma side wall interactions. For the standard base-case ARC operation, ARC is well within the first regime, with a particle flux ratio of ~ 0.5 .

The magnitude of the D coefficient in the outer leg was varied from the base value of $0.25 \text{ m}^2 \text{ s}^{-1}$ across a range of $0.025\text{--}0.4 \text{ m}^2 \text{ s}^{-1}$, with the impact on the downswing detachment threshold shown in figure 16(b). These show a decrease in detachment threshold as D is increased. Except for the data point at $D = 0.025 \text{ m}^2 \text{ s}^{-1}$, the changes are relatively small ($\sim 30\%$), scanning the a wide range of $D = 0.1\text{--}0.4 \text{ m}^2 \text{ s}^{-1}$, so our solutions are seen to be to be fairly robust to variation in D as well.

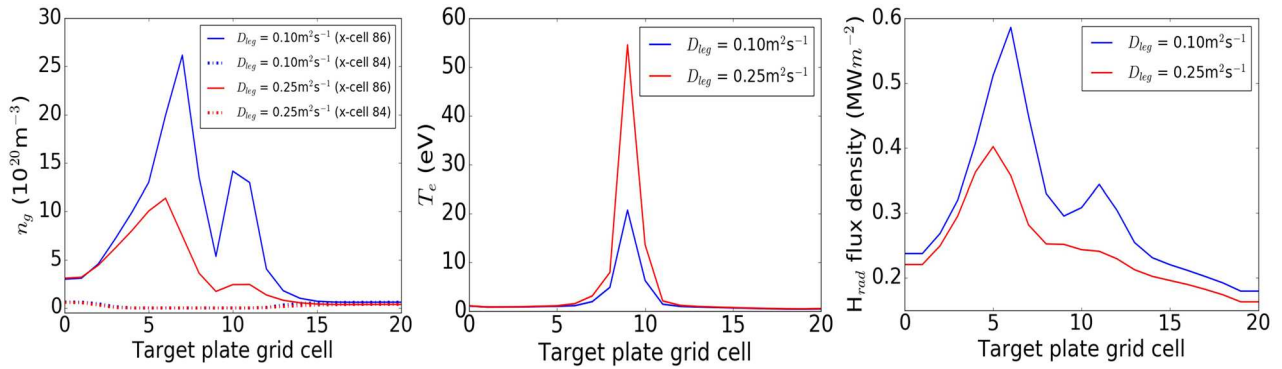


Figure 20. Plots of (left) n_g at the target plate (x-cell = 86) and two cells away from the target (x-cell = 84), (middle) T_e at the target plate, and (right) hydrogenic radiation power flux density on the target plate, for D_{leg} values of $0.1 \text{ m}^2 \text{ s}^{-1}$ (blue) and $0.25 \text{ m}^2 \text{ s}^{-1}$ (red).

The observation that the detachment threshold decreases with increasing D goes against intuitive expectations. One might expect that a smaller D , and hence more concentrated plasma flux, would result in a more concentrated power loading on the divertor and deteriorating divertor power handling performance, not improving. To analyse this, plasma particle/power flows to the divertor leg boundaries are examined again (figure 19). Density profiles are narrower and more peaked with smaller D , resulting in lower particle flux to the side walls and higher particle flux to the divertor targets. However, the plasma power to the primary target has decreased, a result which is again counter-intuitive.

To explain this, we look for any changing conditions at the target plate between the two cases. With high particle flux to this plate and a recycling coefficient of 1.0, the greater flux to the plate from reducing D means greater number of recycled neutrals at the target. This is seen in the simulation as higher neutral density at the target plate, resulting in a factor of ~ 2.5 increase in peak neutral density as D is decreased from 0.25 to $0.1 \text{ m}^2 \text{ s}^{-1}$ (figure 20). The increased neutral density for the $0.1 \text{ m}^2 \text{ s}^{-1}$ case is not seen to extend further into the domain, indicating ionisation of these and enhanced ionisation energy losses. As a result, the peak target temperature drops by factor of ~ 2.8 and peak hydrogenic radiation power flux to the wall increases by factor of ~ 1.5 . This result highlights that for regimes in which the heat and particle transport is primarily directed along field lines to the target plate, the detachment threshold is heavily influenced by the plasma density, neutral densities and recycling fluxes at the target plate, which can be enhanced by reducing cross-field particle transport (D) in high recycling fraction scenarios.

5.3. HFS:LFS power split

In order to access the I-mode confinement regime, a slightly unbalanced double-null equilibrium is found to be required [46, 48], suppressing the formation of H-mode. As a result, the assumed HFS:LFS power split of 10:90 based on a balanced double null configuration may be overly optimistic. Moreover, loss of control of the double-null flux balance could result in an increase in power delivered to the HFS region and the inner divertor target. To test how ARC may perform in such a scenario, power splits of 15:85 and 20:80 are investigated for the 0.57 mm separation XPTD grid, $n_{sep} = 1.2 \times 10^{20} \text{ m}^{-3}$ case

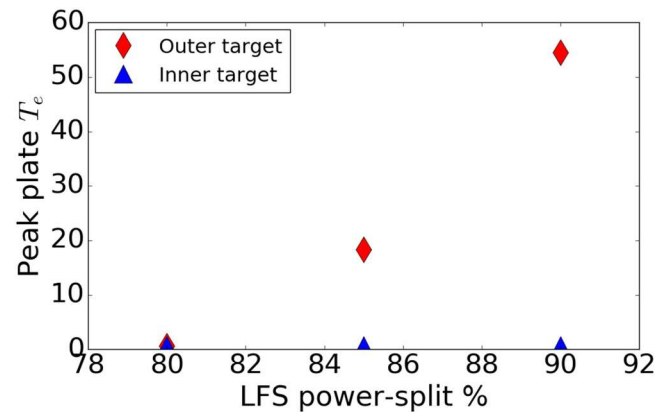


Figure 21. Plot of peak plate temperature (eV) at the inner and outer divertor targets for power split ratios of 10:90, 15:85 and 20:80.

from section 5.1 at the full $P_{SOL} = 105 \text{ MW}$ base value, by adjusting the depth of the $\chi_{i,e}$ transport barrier on the HFS.

The peak plate temperature on the outer and inner divertor targets for the three HFS:LFS power splits investigated are plotted in figure 21. Across the HFS:LFS ratio scan, the outer target moves from an attached to detached state, whilst the inner target remains detached throughout. However, calculating the peak power fluxes to these boundaries (figure 22), we see the peak power flux in all cases for the inner divertor target is above the 10 MW m^{-2} limit, despite remaining detached. The peak power flux at the inner target increases by a factor of ~ 3 for the 80:20 power split ratio compared to 90:10 split. The low plate temperature, detached state at this plate appears to be maintained by extremely high plasma and neutral density in the cells directly above the plate, radiating much of the exhaust power as hydrogenic radiation. This raises questions about the validity of these solutions at the inner divertor target, and more attention may need to be given to the modelling in this region.

6. Discussion

6.1. Long-legged divertor performance

This initial performance assessment of SXD and XPTD divertor configurations for the ARC reactor concept is very

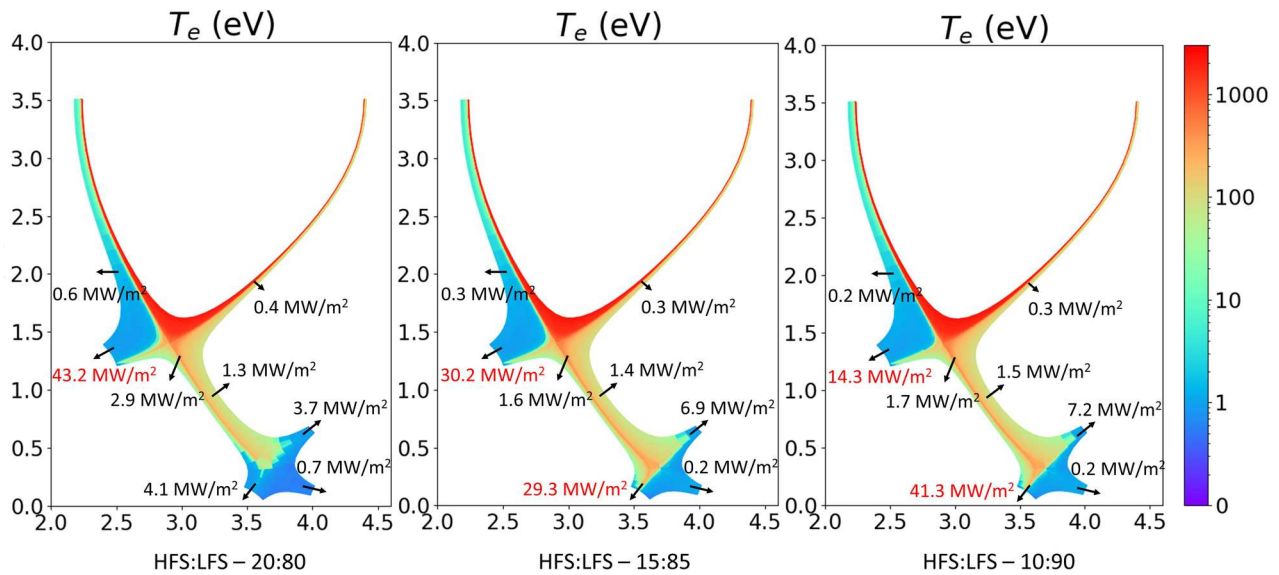


Figure 22. Peak power flux densities to domain boundaries for the $P_{\text{SOL}} = 105$ MW, $n_{\text{sep}} = 1.17 \times 10^{20} \text{ m}^{-3}$ solutions with HFS:LFS power exhaust splits of 20:80 (left), 15:85 (middle) and 10:90 (right).

encouraging—notwithstanding the approximations and simplifications used in the UEDGE simulations. Stable, detached solutions for both the SXD and XPTD grids were obtained at high core exhaust power—in some cases with parallel heat fluxes entering into the divertor of $q_{\parallel} \sim 15 \text{ GW m}^{-2}$ and heat flux widths of $\lambda_{q_{\parallel}} \sim 0.4$ mm, consistent with the anticipated heat flux width for ARC based on empirical scalings.

6.2. SXD

With assistance from the divertor radiation associated with a 0.5% Ne fixed impurity fraction, the SXD was able to achieve stable, fully detached divertor conditions with acceptable first wall power flux loading at the maximum ARC design point exhaust power, $P_{\text{SOL}} = 105$ MW, and a power flux width of $\lambda_{q_{\parallel}} \sim 0.55$ mm measured at the entrance to the divertor. Reducing $\lambda_{q_{\parallel}}$ to 0.4 mm will likely require an increased level of impurity seeding to handle the same power. On the other hand, the leg length of the SXD model mesh did not fully utilize the space available in ARC (see figure 2); extending the leg may provide the necessary performance enhancement. The detached divertor solution identified here relies on the formation of a high-intensity Ne radiation front, which forms directly above the target plate. Peak emissivities on the order of $\sim 850 \text{ MW m}^{-3}$ are observed in the simulation, leading to radiant power loads of $\sim 6 \text{ MW m}^{-2}$ to the target plate, which may be acceptable.

Also associated with Ne seeding is an hysteresis effect observed in the relationship between exhaust power and onset of divertor detachment. While this result is not unexpected, it points to a challenging engineering problem. Detached solutions obtained at the highest power, i.e. the ‘cold branch solutions’ were accessed here by starting from detached solutions at low power and growing them to high power—taking a path through parameter space (e.g. impurity seeding fraction) that maintained plasma detachment. Once the divertor reattached

at the highest powers, the detached state could not be easily regained; it required reducing P_{SOL} to very low power. If this situation is realized in a reactor, power exhaust transients that are able to burn through the detached state would need to be entirely eliminated, and/or a robust mitigation strategy would need to be implemented so as to promptly regain divertor detachment and avoid divertor damage.

6.3. XPTD

This UEDGE modelling assessment shows that a secondary X-point in the divertor leg has potential to significantly enhance divertor performance relative to the SXD case. The base case for the XPTD was set up to be identical to the impurity-free SXD case, except that, due to enhanced grid resolution around the separatrix in the narrowest X-point separation cases, $\lambda_{q_{\parallel}} \sim 0.4$ mm was obtained in the model. Two effects emerge as the magnetic separation between main X-point and divertor X-point flux surfaces, s_x , is reduced: (1) slight increase in divertor detachment power threshold and (2) significant decrease in divertor target electron temperatures under attached divertor conditions, by almost a factor of 10.

An increase in divertor detachment power threshold with decreasing s_x for the XTPD was expected based on previous work using ADX parameters [16, 25]. However, the ARC cases studied thus far have not obtained the factor of ~ 2 enhancement in detachment power threshold seen in the ADX cases—only a 25%–50% enhancement is obtained here (figure 9). This can be attributed to the fact that the X-point separation distance, s_x , normalized to $\lambda_{q_{\parallel}}$ was explored only over the range of $s_x/\lambda_{q_{\parallel}} \sim 3.1$ –1.4, while the ADX study [25] had $s_x/\lambda_{q_{\parallel}} \sim 0.7$. The lack of a factor of 2 enhancement is therefore consistent with the expectation that the secondary X-point should have maximal impact when it most fully intercepts the parallel heat flow channel.

The trend of a decreasing attached divertor target electron temperatures with decreasing $s_x/\lambda_{q||}$ (figure 10) also hints that there may be a large gain in divertor detachment power threshold once $s_x/\lambda_{q||}$ is decreased to ~ 1 . However, the physics that drives this trend appears to be related to the role that the divertor X-point plays in splitting the power channel in to two and narrowing the primary power channel (figure 11). Further study is needed.

With upstream separatrix density elevated above the reference value ($1 \times 10^{20} \text{ m}^{-3}$) to $1.5 \times 10^{20} \text{ m}^{-3}$, the performance of the XPTD is projected to be quite impressive—fully accommodating the ARC exhaust power without any impurity seeding. To our knowledge, this is the first time an impurity-free divertor power handling scenario has been obtained in edge modelling for a tokamak fusion reactor. In view of the potentially dangerous hysteresis effect seen in the detachment power thresholds for the Ne-seeded SXD cases, it may be necessary to operate these divertor configurations with very low or no divertor impurity seeding. In this regard, the identification of a divertor scheme that can successfully operate this way is essential. Needless to say, such a scenario would also be highly beneficial for optimizing the plasma core—reduced core impurity line radiation, reduced Z_{eff} and bremsstrahlung radiation, reduced fuel dilution—and, based on recent results [55], may be in fact be necessary for attaining the I-mode confinement regime.

The insensitivity of the modelling results to the assumed magnitude and mix of convective versus diffusive cross-field particle fluxes in the divertor leg (section 5.2) is encouraging, accommodating a factor of ~ 4 or more variation in the magnitude of each (figure 16). Nevertheless, until experiments can provide definitive data on these parameters—and at the plasma conditions that are projected for the ARC divertor (e.g. plasma density, temperature, neutral densities, heat fluxes)—there will always be uncertainty in these types of model projections.

In summary, we believe that this initial performance assessment of the XPTD concept for ARC is very encouraging, motivating further studies, in particular for the regime $s_x/\lambda_{q||} < 1.4$.

6.4. Model improvements and opportunities for further study

6.4.1. Exploration of reduced X-point separation normalised to $\lambda_{q||}$. The primary goal of the present study was to determine if a viable divertor solution might exist for ARC given its high projected exhaust power (93 MW, assuming 35% core radiation), narrow scrape-off layer heat flux width (0.4 mm) and moderate separatrix density ($1 \times 10^{20} \text{ m}^{-3}$). Thus the present study was constrained to explore models in which $\lambda_{q||}$ was held fixed at 0.4 mm and, for the XPTD, to vary the distance between main X-point and divertor X-point flux surfaces, s_x . This made it impractical to explore the interesting regime of $s_x/\lambda_{q||} < 1.5$ because the present methods used were not able to generate a viable mesh with a secondary X-point for such narrow radial grid spacings. Another approach would be fix s_x and vary $\lambda_{q||}$. This would not reproduce the ARC base-case conditions explored here but it would allow a relative performance assessment of the XPTD that sweeps a wider range

$s_x/\lambda_{q||}$. In addition, the power exhaust could be adjusted so as to hold $q_{||}$ entering into the divertor fixed while $\lambda_{q||}$ is varied.

An exploration of the physics responsible for the trend of a decreasing divertor target electron temperatures in the attached state with decreasing $s_x/\lambda_{q||}$ (figure 10) was beyond the scope of the present investigation; it clearly needs further study. Related to this is the reduction in slope of the T_e versus P_{SOL} trend lines in figures 8 and 9 under attached conditions for decreased values of $s_x/\lambda_{q||}$. It is not clear why the power threshold for detachment is largely insensitive to $s_x/\lambda_{q||}$ while these other parameters vary with $s_x/\lambda_{q||}$ in this regime.

It would also be interesting to examine the case when s_x is exactly zero and to explore negative values of s_x . While the former is not possible with the present version of UEDGE, the latter is. Another possibility is to add yet another X-point to the divertor leg, producing a ‘snowflake target divertor’. But, the magnetic topology of this divertor plus the core plasma configuration is well beyond the capabilities of the present UEDGE code.

6.4.2. Feasibility of controlling and holding X-point separation at $s_x/\lambda_{q||} \sim 1$. Although there may be significant benefit in operating an XPTD with $s_x/\lambda_{q||} \sim 1$, it remains to be determined whether this would be feasible for a plasma shape control system. For reference, an X-point separation of $1 \lambda_{q||}$ ($\sim 0.4 \text{ mm}$) in poloidal flux at the outer midplane maps to a physical separation of $\sim 10 \text{ cm}$ at the vicinity of the X-point target. Thus the location of the divertor X-point may be required to be positioned well within 0.1 m in the ARC tokamak that has a major radius of 3.3 m.

6.4.3. Increasing the radial grid resolution. Due to the challenging nature of the simulations with very narrow SOL widths ($\sim 0.4 \text{ mm}$), the resulting radial grid resolution that could be obtained in these simulations was low. Even for the narrowest XPTD X-point spacings, the resolution only allowed for 2–3 radial grid points to be contained within the first $\lambda_{q||}$ width. This relatively poor radial resolution may have quantitative impact on the modelling results, and it may be the case that a number of our conclusions are subject to change if greater resolution is achieved. Therefore, any further work on this study should make a high priority of increasing the radial resolution, particularly around the separatrix, to verify the results of this paper.

6.4.4. Improved impurity model; inclusion of helium impurity. The magnitude of the detachment power threshold hysteresis effect seen for the Ne seeded case could be due in part to the fixed fraction impurity model that was implemented in UEDGE. Since in this model the local impurity density is strictly proportional to local plasma density, the impurity radiation power is directly coupled to the attached/detached conditions at the target plate, and the associated fall/rise in plasma density near the plate. Implementing a multi-charge state impurity-transport model in UEDGE is the obvious next step for impurity seeded cases, both for improving the impurity radiation power estimates in the divertor and also for examining its impact on divertor detachment power hysteresis. In

addition, helium as a radiating impurity species in the divertor has not been considered in the modelling thus far, despite the fact that helium ash will be present in a fusion tokamak exhaust.

6.4.5. Exploration of inner divertor response and potential inner divertor solutions. In all the simulations performed the inner divertor was always detached within a few cells of the target plate, including cases in which the plasma power delivered to the HFS was set to be high, such as the case in which an 20:80 power split between inner/outer divertor targets is considered (left panel in figure 22). This is because the model produced a very high plasma/neutral density near the target plate resulting in an extremely large fraction of the plasma power being radiated. It is not clear that such a situation is plausible because it has not been seen in present experiments (although present experiments do not approach the plasma pressures and parallel heat fluxes modeled here). One cannot rule out that additional physics, such as enhanced plasma turbulence, might intervene to disperse the high density and cause the inner divertor to reattach. If so, the divertor target, which is a simple flat plate design at present, may need to be redesigned to accommodate it. In any case, we do not believe that this inner divertor behavior significantly impacts the results of the outer divertor scoping study presented in this paper.

6.4.6. Improved neutral model. A simple diffusive neutral transport model was employed for these scoping studies. The use of a fluid model can be justified in this case because the neutral mean-free-path is short compared to the divertor dimensions and gradient scale lengths of plasma parameters in the divertor. The next level of model refinement would be to employ a full Navier–Stokes fluid model that includes inertial terms. Such corrections are important when plasma flows over large regions of the divertor approach sound speed velocities. Indeed we do observe such features in our simulations, particularly in the region between at detachment fronts and a target plate. It is unknown at this time what impact, if any, such corrections have on the divertor detachment power threshold. The use of a Navier–Stokes neutral model for these studies was considered initially but abandoned because converged solutions were not readily obtained and the numerical burden of carrying this forward would have severely hampered this initial scoping study. Ultimately, kinetic neutral models should be employed, fully resolving atomic and molecular species, and assessing the impact of this physics, if any, on the divertor power handling response.

6.4.7. Inclusion of neutral pumping. Helium ash formed by D-T fusion must be continuously removed from the reactor. This is normally facilitated by pumping some small fraction of the neutral recycling flux that appears in the divertor. Our present model does not account for this; it assumes a plasma recycling coefficient of 1 on all surfaces. The next level of refinement in the model is to drop the recycling coefficient below 1 over some region of the divertor leg and re-introduce neutrals elsewhere, according to the fueling method used (e.g.

gas puff, pellets). Based on results from long-legged divertor modelling for the ADX tokamak [25], we expect that the divertor power handling performance of both the SXD and XPTD configurations will experience some degradation as plasma recycling is reduced below unity to simulate the pumping required for helium ash removal. This needs to be quantified for ARC parameters.

6.4.8. Up–down asymmetries and $E \times B$ effects. For the purposes of simplification in this scoping study, we considered perfect up–down symmetry in the boundary plasma and employed a half-domain geometry. Such a situation is clearly not realistic; there will always be a slight up–down imbalance in the geometry and/or there may be a need to operate with an up–down imbalance, such as to access an I-mode confinement regime with ∇B drift away from the primary main plasma X-point. A result of this will be an enhanced power load to the primary divertor, which can significantly impact the overall level of exhaust power that the divertors can handle. Additionally, our model does not include particle drift effects, most notably, $E \times B$ drift effects, which are known to affect divertor detachment responses [56]. Hence, inclusion of drifts may have notable impact on the conclusions and quantitative results reported in this paper. Further studies are needed to assess the potential impact of both these effects on the power handling limits of both the SXD and XPTD configurations under ARC parameters.

7. Summary and conclusion

The performance of long-legged, tightly baffled divertor configurations in application to the ARC fusion reactor concept [20] has been studied for the first time using the UEDGE edge plasma transport code [26]. Both Super-X divertor (SXD) [10] and X-point target divertor (XPTD) [14] configurations were explored, with the latter being the baseline divertor configuration considered for ARC [22]. Scrape-off layer (SOL) power e-folding widths ($\lambda_{q||}$) are based on empirical data [23, 46], which project to a characteristic $\lambda_{q||}$ value of 0.4 mm, mapped to the outboard midplane. A range of power exhaust was explored, accommodating the baseline operational scenario for ARC (35% core radiation, $P_{\text{SOL}} = 93$ MW) as well as higher power scenarios (105 MW) corresponding to peak parallel heat fluxes entering into the divertor of ~ 10 GW m⁻². SOL density profiles were chosen to correspond to ARC's baseline I-mode scenario, with a nominal separatrix density of 1×10^{20} m⁻³ and a flattened profile in the far SOL, consistent with observations on Alcator C-Mod. The former is based on the assumption of I-mode operation to allow for the separatrix density to be equal to the edge density of the core profiles in the ARC design paper [20], and the latter required certain assumptions about the anomalous plasma transport in the far SOL, consistent with the large body of experimental data obtained on C-Mod and other tokamaks, i.e. the main chamber recycling phenomena due to non-diffusive blob transport of plasma density. It was assumed that similar diffusive and

convective cross-field transport occurred in the divertor leg. Sensitivity studies revealed that divertor solutions obtained were insensitive to diffusive and convective coefficients, admitting more than a factor of 4 variation in each.

Passively-stable, fully-detached divertor solutions were found for both SXD and XPTD configurations, accommodating the full exhaust power of ARC. For the SXD configurations a small Ne impurity ion fraction (0.5%) was required to handle the baseline scenario with separatrix density of $1 \times 10^{20} \text{ m}^{-3}$. This led to a significant hysteresis in relationship between exhaust power level and detachment power threshold ('hot' and 'cold' branch solutions), which may be a concern for handling power exhaust transients. The XPTD configuration was found to have improved power handling compared to the SXD, depending on the spacing between main plasma and divertor X-point flux surfaces. By raising the separatrix density to $1.5 \times 10^{20} \text{ m}^{-3}$, passively-stable, fully-detached divertor solutions were found at X-point separations of $1.5 \times \lambda_{q||}$ —fully accommodating the exhaust power of ARC without the need for any impurity ion radiation at all. Solutions without impurity radiation are particularly attractive as they avoid controversial assumptions about impurity ion impacts and containment in the divertor (which is poorly understood in the present-day machines). Moreover, these solutions did not exhibit a large hysteresis effect in detachment power, making them attractive from a control point of view in which fast power exhaust transients (e.g. H-L transitions) cannot be avoided.

As the spacing between main plasma and divertor X-point flux surfaces approaches the range of $1 \times \lambda_{q||}$, further improvement in XPTD performance is evident: divertor target electron temperatures at full exhaust power (105 MW) drop by a factor of 10. This overall trend projects to the XPTD configuration attaining a passively-stable, fully detached, impurity-free scenario for X-point spacings of $1 \times \lambda_{q||}$ or less. Whilst the modelling has significant shortcomings—particularly regarding poor radial resolution in relation to $\lambda_{q||}$ and the lack of inclusion of drift effects—these results clearly call for further study into this potentially interesting parameter range, as well as to incorporate refinements in the model and to fix its shortcomings, as identified in this paper.

Overall, these results set a new precedent suggesting that it is possible to achieve, in numerical modelling at least, benign power flux levels to plasma facing surfaces of the tightly-baffled, long-legged divertors integrated into the ARC fusion reactor design—accommodating the full level of power exhaust possible, accounting for the narrow heat flux width that is now being projected, meeting the requirements of no or low-impurity seeding levels—and doing so with a passively-stable, hysteresis-free, divertor detachment response.

Acknowledgments

This work has been supported by the University of York, Massachusetts Institute of Technology (supported by US DoE cooperative agreement DE-SC0014264), Lawrence Livermore National Laboratory (supported under DoE

Contract DE-AC52-07NA27344) and the UK Engineering and Physical Science Research Council (EPSRC) as part of the EPSRC Fusion Centre for Doctoral Training programme (under Training Grant Number EP/LO1663X/1). Data supporting this contribution can be found at the DOI: <https://doi.org/10.15124/d7a13911-41dd-4e99-983f-1e62430c9ef4>.

ORCID iDs

M.R.K. Wigram  <https://orcid.org/0000-0002-5376-128X>
 B. LaBombard  <https://orcid.org/0000-0002-7841-9261>
 A.Q. Kuang  <https://orcid.org/0000-0002-8917-2911>
 J.L. Terry  <https://orcid.org/0000-0003-4255-5509>
 D. Brunner  <https://orcid.org/0000-0002-8753-1124>

References

- [1] Pitts R.A. et al 2011 *J. Nucl. Mater.* **415** S957–64
- [2] Loarte A. et al 2007 *Nucl. Fusion* **47** S203
- [3] Mandrekas J. et al 1996 *Nucl. Fusion* **36** 917
- [4] Pitts R.A. et al 2009 *Phys. Scr.* **2009** 014001
- [5] Kukushkin A.S. et al 2009 *Nucl. Fusion* **49** 075008
- [6] Zohm H. et al 2013 *Nucl. Fusion* **53** 073019
- [7] Wischmeier M. et al 2015 *J. Nucl. Mater.* **463** 22–9
- [8] Soukhanovskii V.A. 2017 *Plasma Phys. Control. Fusion* **59** 064005
- [9] Brunner D., Kuang A.Q., LaBombard B. and Terry J.L. 2018 *Nucl. Fusion* **58** 076010
- [10] Valanju P.M., Kotschenreuther M., Mahajan S.M. and Canik J. 2009 *Phys. Plasmas* **16** 056110
- [11] Katramados I. et al 2011 *Fusion Eng. Des.* **86** 1595–8
- [12] Kotschenreuther M. et al 2004 Scrape off layer physics for burning plasmas and innovative divertor solutions *Proc. 20th IAEA Fusion Energy Conf. (Vilamoura, Portugal, 1–6 November 2004)* IC/P6-43 (<http://www-naweb.iaea.org/naweb/physics/fec/fec2004/datasets/index.html>)
- [13] Ryutov D.D. and Soukhanovskii V.A. 2015 *Phys. Plasmas* **22** 110901
- [14] LaBombard B. et al 2015 *Nucl. Fusion* **55** 053020
- [15] Meier E.T. et al 2015 *J. Nucl. Mater.* **463** 1200–4
- [16] Umansky M.V. et al 2017 *Nucl. Mater. Energy* **12** 918–23
- [17] Theiler C. et al 2017 *Nucl. Fusion* **57** 072008
- [18] Reimerdes H. et al 2015 Towards an assessment of alternative divertor solutions for DEMO *42nd EPS Conf. on Plasma Physics (Lisbon, Portugal, 22–26 June 2015)* P4.117 (<http://www-naweb.iaea.org/naweb/physics/fec/fec2004/datasets/index.html>)
- [19] Lackner K. and Zohm H. 2013 *Fusion Sci. Technol.* **63** 43
- [20] Sorbom B.N. et al 2015 *Fusion Eng. Des.* **100** 378–405
- [21] Hartwig Z.S., Haakonsen C.B., Mumgaard R.T. and Bromberg L. 2012 *Fusion Eng. Des.* **87** 201–14
- [22] Kuang A.Q. et al 2018 *Fusion Eng. Des.* **137** 221
- [23] Eich T. et al 2013 *Nucl. Fusion* **53** 093031
- [24] Whyte D.G. et al 2016 *J. Fusion Energy* **35** 41
- [25] Umansky M.V. et al 2017 *Phys. Plasmas* **24** 056112
- [26] Rognlien T.D., Milovich J.L., Rensink M.E. and Porter G.D. 1992 *J. Nucl. Mater.* **196–8** 347
- [27] Rognlien T.D., Ryutov D.D., Mattor N. and Porter G.D. 1999 *Phys. Plasmas* **6** 1851
- [28] Rognlien T.D. and Rensink M.E. 2002 *Fusion Eng. Des.* **60** 497–514
- [29] Wising F. et al 1996 *Contrib. Plasma Phys.* **36** 309–13
- [30] Rensink M.E. et al 2007 *J. Nucl. Mater.* **363–5** 816

- [31] Christem N. *et al* 2017 *Plasma Phys. Control. Fusion* **59** 105004
- [32] Umansky M.V. *et al* 2009 *Nucl. Fusion* **49** 075005
- [33] Tani K., Azumi M. and Devoto R.S. 1992 *J. Comput. Phys.* **98** 332
- [34] Devoto R.S. *et al* 1992 *Nucl. Fusion* **32** 773
- [35] Rognlien T.D. *et al* 2010 Advances in understanding tokamaks edge/scrape-off layer transport *Proc. 23rd IAEA Fusion Energy Conf. (Daejeon, Republic of Korea, 11–16 October 2010)* THD/P3-05 (<http://www-naweb.iaea.org/napc/physics/FEC/FEC2010/index.htm>)
- [36] Whyte D.G. *et al* 2010 *Nucl. Fusion* **50** 105005
- [37] LaBombard B. *et al* 2001 *Phys. Plasmas* **8** 5
- [38] LaBombard B. *et al* 2005 *Nucl. Fusion* **45** 1658–75
- [39] LaBombard B. *et al* 2000 *Nucl. Fusion* **40** 12
- [40] Krasheninnikov S.I. 2001 *Phys. Lett. A* **283** 368
- [41] Dippolito D.A. and Myra J.R. 2001 *Phys. Plasmas* **9** 222
- [42] Kukuskin A.S. *et al* 2001 *J. Nucl. Mater.* **290–3** 887–91
- [43] Harrison J.M., Fishpool G.M. and Dudson B.D. 2015 *J. Nucl. Mater.* **463** 757–60
- [44] Scotti F. *et al* 2018 *Nucl. Fusion* **58** 126028
- [45] LaBombard B. *et al* 2004 *Nucl. Fusion* **44** 1047
- [46] Brunner D., LaBombard B., Kuang A.Q. and Terry J.L. 2018 *Nucl. Fusion* **58** 094002
- [47] Erents S.K. and Stangeby P.C. 1998 *Nucl. Fusion* **38** 1637
- [48] Hubbard A.E. *et al* 2017 *Nucl. Fusion* **57** 126039
- [49] Umansky M.V. *et al* 1999 *Phys. Plasmas* **6** 2791
- [50] Kirk A. *et al* 2004 *Plasma Phys. Control. Fusion* **46** 551
- [51] Umansky M.V., Krasheninnikov S.I., LaBombard B. and Terry J.L. 1998 *Phys. Plasmas* **5** 3373
- [52] Wigram M. *et al* 2018 *Contrib. Plasma Phys.* **58** 791–7
- [53] Krasheninnikov S.I. *et al* 1995 *Phys. Plasmas* **2** 2717
- [54] Sun H.J. *et al* 2017 *Plasma Phys. Control. Fusion* **59** 105010
- [55] Reinke M.L. *et al* 2019 *Nucl. Fusion* **59** 046018
- [56] Hutchinson I.H. *et al* 1995 *Plasma Phys. Control. Fusion* **37** 1389